

# Coagulation Calculations of Icy Planet Formation at 15–150 AU: A Correlation Between the Maximum Radius and the Slope of the Size Distribution for Transneptunian Objects

Scott J. Kenyon

*Smithsonian Astrophysical Observatory, 60 Garden Street, Cambridge, MA 02138*

e-mail: skenyon@cfa.harvard.edu

Benjamin C. Bromley

*Department of Physics, University of Utah, 201 JFB, Salt Lake City, UT 84112*

e-mail: bromley@physics.utah.edu

## ABSTRACT

We investigate whether coagulation models of planet formation can explain the observed size distributions of transneptunian objects (TNOs). Analyzing published and new calculations, we demonstrate robust relations between the size of the largest object and the slope of the size distribution for sizes 0.1 km and larger. These relations yield clear, testable predictions for TNOs and other icy objects throughout the solar system. Applying our results to existing observations, we show that a broad range of initial disk masses, planetesimal sizes, and fragmentation parameters can explain the data. Adding dynamical constraints on the initial semimajor axis of ‘hot’ KBOs along with probable TNO formation times of 10–700 Myr restricts the viable models to those with a massive disk composed of relatively small (1–10 km) planetesimals.

*Subject headings:* Planetary systems – Planets and satellites: formation – Planets and satellites: physical evolution – Kuiper belt: general

## 1. INTRODUCTION

The transneptunian objects (TNOs, small icy planets orbiting the Sun beyond Neptune) provide crucial tests of planet formation theories. With its rich dynamical structure, the current orbital architecture of TNOs constrains models for the dynamical interactions among

newly-formed gas giants and for the origin of the Oort cloud (e.g., Morbidelli et al. 2008). The diverse populations of binary TNOs provide additional constraints on the dynamical history of the solar system (Noll et al. 2008; Nesvorný et al. 2011; Murray-Clay & Schlichting 2011). Finally, the sizes of the largest TNOs and the size distributions within the dynamical families of TNOs constrain the formation histories of the gas giants, the TNOs, and perhaps the terrestrial planets (e.g., Kenyon & Luu 1998; Kenyon 2002; Gomes et al. 2005; Morbidelli et al. 2008).

There are two broad concepts for the formation and evolution of TNOs. Both begin with small dust grains within a massive gaseous disk surrounding a young star. As the disk evolves, dust grains collide, merge, and grow into mm- to cm-sized objects which decouple from the gas and fall into the midplane of the disk (e.g., Birnstiel et al. 2010, and references therein). Once a large fraction of the solid material is in the midplane, the two paths to TNOs diverge. In one path, icy objects continue to collide, merge, and grow into roughly km-sized planetesimals and then into much larger TNOs (e.g., Weidenschilling 1997). In the other path, instabilities or turbulent eddies in the disk concentrate icy objects into massive clumps which collapse directly into large TNOs (e.g., Johansen et al. 2007; Chambers 2010; Cuzzi et al. 2010; Pan et al. 2011). Once TNOs form, the evolutionary paths converge: dynamical interactions with the gas giants produce the diverse architecture of the current TNO population (e.g., Morbidelli et al. 2008).

Testing the two formation paths requires robust theoretical models which make clear predictions for the maximum radius and the size distribution of TNOs. At present, analytic theory and numerical simulations cannot predict the outcome of instability mechanisms (Chiang & Youdin 2010; Pan et al. 2011). However, coagulation models yield robust predictions for the time evolution of the size distribution and the sizes of the largest objects (e.g., Kenyon & Luu 1999a; Kenyon 2002; Kenyon & Bromley 2004c; Kenyon et al. 2008, and references therein). Thus, it is possible to compare the results of coagulation calculations with the observable properties of TNOs (Kenyon & Luu 1999b; Kenyon & Bromley 2004c; Fraser 2009).

To test the coagulation model in detail, we analyze a set of published (Kenyon & Bromley 2008, 2010) and new coagulation calculations. Our numerical models follow the collisional and dynamical evolution of small planetesimals into TNOs at orbital semimajor axes  $a = 15\text{--}150$  AU for evolution times 1–10 Gyr. This range of semimajor axes lies outside the most likely region of giant planet formation (e.g., Rafikov 2004; Goldreich et al. 2004; Kennedy & Kenyon 2008; Kenyon & Bromley 2009). By considering a broad range of initial planetesimal sizes (and size distributions) and a range of fragmentation parameters, we derive the time evolution of the radius of the largest object and the slope of the size distribution

as a function of initial conditions and distance from the Sun. Comparisons of our results with the observations allows an assessment of the match between the observed properties of TNOs and the models.

Coagulation models yield robust predictions for the relation between the size of the largest object and the slope of the size distribution. Although this relation is insensitive to distance from the Sun and fairly insensitive to the fragmentation parameters, the evolution depends on the initial disk mass, the initial size of the largest planetesimals, and the initial size distribution of planetesimals.

Using recent observations from large surveys of TNOs, we demonstrate that collisional evolution often yields size distributions similar to those observed. On their own, the observations favor models with 1–10 km planetesimals relative to those with 100 km planetesimals. Adding dynamical constraints on the origin of the hot and cold populations of KBOs to our analysis, we show that models in (i) massive disks with 1 km planetesimals and (ii) low mass disks with 10 km planetesimals provide equally satisfactory matches to the data. Requiring that TNOs form prior to the Late Heavy Bombardment eliminates models with low mass disks. Thus, all of the available data taken together imply that TNOs formed in a massive disk composed of 1 km planetesimals.

We begin our discussion with an overview of the numerical code in §2. After describing basic results of the calculations in §3, we compare the results with observations in §4. We conclude with a brief summary in §5.

## 2. PLANET FORMATION CALCULATIONS

To calculate the formation and evolution of TNOs, we use a hybrid multiannulus coagulation– $N$ -body code. We compute the collisional evolution of an ensemble of planetesimals in a circumstellar disk orbiting a central star of mass  $M_\star$ . The code uses statistical algorithms to evolve the mass and velocity distributions of low mass objects with time and an  $N$ -body algorithm to follow the individual trajectories of massive objects. Kenyon & Bromley (2008) describe the statistical (coagulation) code; Bromley & Kenyon (2006) describe the  $N$ -body code. Here, we briefly summarize the basic aspects of our approach.

We perform calculations on a cylindrical grid with inner radius  $a_{in}$  and outer radius  $a_{out}$  surrounding a star with  $M_\star = 1 M_\odot$ . The model grid contains  $N$  concentric annuli with widths  $\delta a_i = 0.025 a_i$  centered at semimajor axes  $a_i$ . Calculations begin with a cumulative mass distribution  $n_c(m_{ik}) \propto m_{ik}^{-q_{init}}$  of planetesimals with mass density  $\rho_p = 1.5 \text{ g cm}^{-3}$  and maximum initial mass  $m_0$ . Although our code explicitly tracks the mass distribution

of solid objects, in the rest of the text we describe initial conditions and results in terms of cumulative size distributions,  $n_c(r)$ . For a power law cumulative size distribution,  $n_c \propto r^{-q}$ , the power-law exponent is a factor of 3 larger than the exponent for the mass distribution. Thus,  $q_{init} = 3q'_{init}$ . For this paper, we adopt  $q_{init} = 0.5$  (most of the mass in the largest planetesimals) and 3.0 (mass distributed equally per logarithmic interval in mass/radius).

Planetesimals have horizontal and vertical velocities  $h_{ik}(t)$  and  $v_{ik}(t)$  relative to a circular orbit. The horizontal velocity is related to the orbital eccentricity,  $e_{ik}^2(t) = 1.6 (h_{ik}(t)/V_{K,i})^2$ , where  $V_{K,i}$  is the circular orbital velocity in annulus  $i$ . The orbital inclination depends on the vertical velocity,  $i_{ik}^2(t) = \sin^{-2}(2(v_{ik}(t)/V_{K,i}))$ .

The mass and velocity distributions of the planetesimals evolve in time due to inelastic collisions, drag forces, and gravitational encounters. As summarized in Kenyon & Bromley (2004a, 2008), we solve a coupled set of coagulation equations which treats the outcomes of mutual collisions between all particles with mass  $m_j$  in annuli  $a_i$ . We adopt the particle-in-a-box algorithm, where the physical collision rate is  $n\sigma v f_g$ ,  $n$  is the number density of objects,  $\sigma$  is the geometric cross-section,  $v$  is the relative velocity, and  $f_g$  is the gravitational focusing factor (Safronov 1969; Lissauer 1987; Spaute et al. 1991; Wetherill & Stewart 1993; Weidenschilling et al. 1997; Kenyon & Luu 1998; Kenyon & Bromley 2008). For a specific mass bin, our solutions include terms for (i) loss of mass from gas drag and mergers with other objects and (ii) gain of mass from collisional debris and mergers of smaller objects.

Aside from deriving the cross-section and relative collision velocity, the main ingredient in this calculation is the gravitational focusing factor for a collision between two planetesimals with masses (radii)  $m_i$  and  $m_j$  ( $r_i$  and  $r_j$ ). In the high velocity, dispersion-dominated regime, we adopt a variant of the piecewise analytic approximation of Spaute et al. (1991, see also Kenyon & Luu 1998):

$$f_{g,d} = \begin{cases} 1 + \beta(v_e/v)^2 & v > 0.32v_e, \\ 42.4042 (v_e/v)^{1.2} & 0.01 < v/v_e \leq 0.32, \\ 10651.453 & v/v_e \leq 0.01, \end{cases} \quad (1)$$

where  $\beta$  is an order unity constant which accounts for the distribution of impact velocities (Greenzweig & Lissauer 1992),  $v$  is the velocity of a planetesimal, and  $v_e$  is the escape velocity of the merged pair of planetesimals.

For the low velocity, shear-dominated regime, we define the angular velocity  $\Omega = (GM_\star/a^3)^{1/2}$ , the Hill radius  $r_H = a(m/3M_\odot)^{1/3}$ , the Hill velocity  $v_H = \Omega r_H$ , and an angular scale factor  $\psi = (\rho_\odot/\rho_p)^{1/3} R_\odot/a$ , where  $\rho_\odot$  is the mean density of the Sun and  $R_\odot$  is the

solar radius. In the Greenberg et al. (1991) approach,

$$f_{g,s} = \begin{cases} (1 + v_e^2/v_T^2)(v_T/v)(r_H/r_T) & v \lesssim v_H, \\ 0.5(1 + v_e^2/v_T^2)^{1/2}(v_T/v)(r_H/r_T)(H/(r_i + r_j)) & v \lesssim v_H, v \lesssim \psi^{1/2}v_H \end{cases} \quad (2)$$

where  $r_T = a((m_i + m_j)/m_\star)^{2/5}$  is the Tisserand radius,  $v_T = 1.1\Omega\delta a_T$  is the Tisserand velocity, and  $H$  is the vertical scale height of the planetesimals. In the Goldreich et al. (2004) approach,

$$f_{g,s} = \begin{cases} \psi^{-1}(v_h/v) & v \lesssim v_H, \\ \alpha^{-3/2} & v \lesssim v_H, v \lesssim \psi^{1/2}v_H \end{cases} \quad (3)$$

Tests using both approaches yield similar results for the collision rate. The simpler Goldreich et al. (2004) relations are computationally cheaper. For either approach, we employ a simple algorithm to affect a smooth transition in  $f_g$  between the dispersion and shear rates (Kenyon & Luu 1998). Because  $\psi$  decreases with  $a$ , icy planet formation at 15–150 AU is less likely to enter the shear-dominated regime than rocky planet formation at 1 AU.

Collision outcomes depend on the ratio  $Q_c/Q_D^*$ , where  $Q_D^*$  is the collision energy needed to eject half the mass of a pair of colliding planetesimals to infinity and  $Q_c$  is the center of mass collision energy. For two colliding planetesimals with masses  $m_1$  and  $m_2$ , the mass of the merged planetesimal is

$$m = m_1 + m_2 - m_{ej}, \quad (4)$$

where the mass of debris ejected in a collision is

$$m_{ej} = 0.5 (m_1 + m_2) \left( \frac{Q_c}{Q_D^*} \right)^{9/8}. \quad (5)$$

To place the debris in our grid of mass bins, we set the mass of the largest collision fragment as  $m_L = 0.2m_{esc}$  and adopt a cumulative size distribution  $n_c \propto r^{-q_d}$  (Davis et al. 1985). Here, we adopt  $q_d = 2.5$ , the value expected for a system in collisional equilibrium (Dohnanyi 1969; Williams & Wetherill 1994; Tanaka & Ida 1996; O’Brien & Greenberg 2003; Kobayashi & Tanaka 2010).

This approach allows us to derive ejected masses for catastrophic collisions with  $Q_c \sim Q_D^*$  and for cratering collisions with  $Q_c \ll Q_D^*$  (see also Wetherill & Stewart 1993; Williams & Wetherill 1994; Tanaka & Ida 1996; Stern & Colwell 1997a; Kenyon & Luu 1999a; O’Brien & Greenberg 2003; Kobayashi & Tanaka 2010). Consistent with N-body simulations of collision outcomes (e.g., Benz & Asphaug 1999; Leinhardt et al. 2008; Leinhardt & Stewart 2009), we set

$$Q_D^* = Q_b r^{\beta_b} + Q_g \rho_p r^{\beta_g} \quad (6)$$

where  $Q_b r^{\beta_b}$  is the bulk component of the binding energy,  $Q_g \rho_p r^{\beta_g}$  is the gravity component of the binding energy, and  $r$  is the radius of a planetesimal.

To explore the sensitivity of our results to the fragmentation algorithm, we consider three sets of parameters  $f_i$  (Fig. 1). As in Kenyon & Bromley (2008, 2010), strong planetesimals have  $f_s = (Q_b = 10^1, 10^3, \text{ or } 10^5 \text{ erg g}^{-1}, \beta_b = 0, Q_g = 2.25 \text{ erg g}^{-2} \text{ cm}^{1.75}, \beta_g = 1.25;$  Benz & Asphaug 1999); weaker planetesimals have  $f_w = (Q_b = 2 \times 10^5 \text{ erg g}^{-1} \text{ cm}^{0.4}, \beta_b = -0.4, Q_g = 0.33 \text{ erg g}^{-2} \text{ cm}^{1.7}, \beta_g = 1.3;$  Leinhardt & Stewart 2009). Here, we also consider a set of very strong planetesimals with  $f_{vs} = (Q_b = 10^1, 10^3, \text{ or } 10^5 \text{ erg g}^{-1}, \beta_b = 0, Q_g = 10^{-4} \text{ erg g}^{-2} \text{ cm}, \beta_g = 2.0;$  e.g., Davis et al. 1985). At small sizes, these parameters are broadly consistent with results from laboratory experiments of impacts with icy targets and projectiles (e.g., Ryan et al. 1999; Arakawa et al. 2002; GIBLIN et al. 2004; Burchell et al. 2005).

For our calculations, these parameters have several consequences. When fragmentation begins, most of the mass is in planetesimals with  $r \approx 1\text{--}100 \text{ km}$ . With  $Q_D^*(r = 1\text{--}100 \text{ km}) > Q_D^*(r = 1\text{--}10^5 \text{ cm})$ , the gravity regime of the fragmentation law sets the collision velocity for the onset of fragmentation. To achieve catastrophic fragmentation with  $Q_c/Q_D^* = 1$ , weak planetesimals require the smallest collision velocity; very strong planetesimals require the largest. In all cases, once large objects begin to fragment, smaller objects also fragment. Thus, the onset of fragmentation for 1–100 km planetesimals initiates a collisional cascade where all small objects are ground to dust.

To compute the evolution of the velocity distribution, we include collisional damping from inelastic collisions, gas drag, and gravitational interactions. For inelastic and elastic collisions, we follow the statistical, Fokker-Planck approaches of Ohtsuki (1992) and Ohtsuki et al. (2002), which treat pairwise interactions (e.g., dynamical friction and viscous stirring) between all objects in all annuli. As in Kenyon & Bromley (2001), we add terms to treat the probability that objects in annulus  $i_1$  interact with objects in annulus  $i_2$  (see also Kenyon & Bromley 2004b, KB08). We also compute long-range stirring from distant oligarchs (Weidenschilling 1989). For gas drag, we derive velocity damping and the inward drift of material in the quadratic, Stokes, and Epstein limits (e.g., Adachi et al. 1976; Weidenschilling 1977a; Rafikov 2004).

To evolve the gas in time, we consider a simple nebular model for the gas density. We adopt a scale height  $H_{gas}(a) = H_{gas,0}(a/a_0)^{1.125}$  (Kenyon & Hartmann 1987) and assume the gas surface density declines exponentially with time

$$\Sigma_{gas}(a, t) = \Sigma_{gas,0} x_m a^{-n} e^{-t/t_{gas}} \quad (7)$$

where  $\Sigma_{gas,0}$  and  $x_m$  are scaling factors and  $t_{gas} = 10 \text{ Myr}$  is the gas depletion time. Although longer than the 2–5 Myr timescale estimated from observations of the lifetimes of accretion disks in pre-main sequence stars (Currie et al. 2009; Kennedy & Kenyon 2009; Mamajek 2009; Williams & Cieza 2011), shorter gas depletion times have little impact on our results.

In the  $N$ -body code, we directly integrate the orbits of objects with masses larger than a pre-set ‘promotion mass’  $m_{pro}$ . The calculations allow for mergers among the  $N$ -bodies. Additional algorithms treat mass accretion from the coagulation grid and mutual gravitational stirring of  $n$ -bodies and mass batches in the coagulation grid. For the applications in this paper, the few large objects capable of promotion into the  $N$ -body code never contain a significant fraction of the mass in an annulus and never contribute significantly to the local stirring. To treat situations where a few large objects might impact the evolution, we set  $m_{pro} = 10^{26}$  g. However, our calculations never produced more than a few  $N$ -bodies which remain on nearly circular orbits throughout their evolution.

The initial conditions for these calculations are appropriate for a disk with an age of  $\lesssim 1$ –2 Myr (e.g., Williams & Cieza 2011, and references therein). We consider systems of  $N = 64$  annuli in disks where the initial surface density of solid material follows a power law in semimajor axis,

$$\Sigma_{d,i} = \Sigma_{d,0}(M_{\star}) x_m a_i^{-n}, \quad (8)$$

where  $a_i$  is the central radius of the annulus in AU,  $n = 1$  or  $3/2$ , and  $x_m$  is a scaling factor. For a standard gas to dust ratio of 100:1,  $\Sigma_{gas,0} = 100 \Sigma_{d,0}(M_{\star})$ . To explore a range of disk masses similar to the observed range among the youngest stars, we consider  $\Sigma_{d,0} = 30 \text{ g cm}^{-2}$  and  $x_m = 0.01$ –3. Disks with  $x_m \approx 0.1$  have masses similar to the median disk masses observed around young stars in nearby dark clouds (Andrews & Williams 2005; Williams & Cieza 2011). Somewhat larger scale factors,  $x_m \approx 1$ , correspond to models of the minimum mass solar nebula models of Weidenschilling (1977b) and Hayashi (1981).

Table 1 summarizes the model grids. For each set of  $x_m$ , we choose the extent of the disk,  $a = 15$ –75 AU or 30–150 AU; initial radius of the largest planetesimal,  $r_0 = 1, 10, 100$  km; the initial eccentricity  $e_0 = 10^{-4}$  and inclination  $i_0 = 5 \times 10^{-5}$ ; the power law exponent of the initial size distribution,  $q_{init} = 3$  (equal mass per log interval in mass) or  $q_{init} = 0.5$  (most of the mass in the largest objects); the fragmentation parameters,  $f_s$ ,  $f_{vs}$ , or  $f_w$ ; and the evolution time  $t_{max}$ . To understand the possible range of outcomes, we repeat calculations 5–15 times for each combination of initial conditions. Kenyon & Bromley (2008, 2010) discuss some aspects of these calculations in the context of observations of debris disks.

Our calculations follow the time evolution of the mass and velocity distributions of objects with a range of radii,  $r_{ij} = r_{min}$  to  $r_{ij} = r_{max}$ . The upper limit  $r_{max}$  is always larger than the largest object in each annulus. To save computer time, we do not consider small objects which do not significantly affect the dynamics and growth of larger objects,  $r_{min} = 100$  cm. Erosive collisions produce objects with  $r_{ij} < r_{min}$  which are ‘lost’ to the model grid. Lost objects are more likely to be ground down into smaller objects than to collide with larger objects in the grid (see Kenyon & Bromley 2002, 2002b, 2004a).

### 3. EVOLUTION OF THE SIZE DISTRIBUTION

At the start of each calculation, dynamical processes drive the evolution. Gas drag damps the velocities of the smallest objects. Dynamical friction damps the orbital velocities of the largest objects; dynamical friction and viscous stirring excite velocities of the smallest objects (Goldreich et al. 2004; Kenyon & Bromley 2008, 2010). With stirring timescales much faster than growth timescales, it takes 10–50 orbits to achieve a relaxed distribution of velocities among all planetesimal sizes. For calculations with  $r_0 = 1$ –10 km, this evolution occurs in the dispersion-dominated regime; dynamics and growth are slow and orderly. When  $r_0 = 100$  km, dynamical evolution rapidly drives the system from the shear regime to the dispersion regime. Thus, initial growth rates for large planetesimals are also slow and orderly.

As the evolution proceeds, dynamical processes produce substantial gravitational focusing factors. Runaway growth begins. The largest objects then grow much more rapidly than, and ‘run away’ from, somewhat smaller protoplanets. The initial stages of this process are in the dispersion regime; accretion in the shear regime dominates the later stages. Throughout this evolution, the largest objects – with radii of 300–1000 km – continue to stir the smallest objects. Stirring reduces gravitational focusing factors, ending shear-dominated accretion and runaway growth. Oligarchic growth in the dispersion regime begins.

Throughout oligarchic growth, protoplanets evolve in two distinct ways. The largest protoplanets – known as oligarchs – accrete material primarily from the reservoir of small planetesimals. Because gravitational focusing factors are small, growth is orderly. Small oligarchs grow faster than large oligarchs. Both grow faster than smaller planetesimals (e.g., Goldreich et al. 2004). As all of the oligarchs grow, they stir the smallest planetesimals to larger and larger orbital velocities. Eventually, collisions among small planetesimals become destructive, producing smaller planetesimals and some debris. Collisions among smaller planetesimals are even more destructive, leading to a collisional cascade where small planetesimals are ground to dust (e.g., Dohnanyi 1969; Williams & Wetherill 1994; Kobayashi & Tanaka 2010; Belyaev & Rafikov 2011, and references therein). By robbing the oligarchs of small planetesimals, the collisional cascade limits the growth of the largest planets to  $\sim 3 - 10 \times 10^3$  km (e.g., Inaba et al. 2003; Kenyon & Bromley 2008, 2010; Kobayashi & Tanaka 2010).

On 1–10 Gyr time scales, the collisional cascade removes most of the initial mass in solids at  $a \lesssim 100$  AU (Kenyon & Bromley 2008, 2010). Kenyon & Bromley (2008) express the fraction of solid material remaining in the disk as  $f_s \approx f_0 x_m^{-1/4} (a/30 \text{ AU})^{5/4}$ . Collisional growth proceeds more rapidly at smaller  $a$  in more massive disks. For a fixed evolution time, the cascade removes more mass at smaller  $a$  and less mass in less massive disks. For calculations with  $r_0 = 1$  km and strong (weak) planetesimals,  $f_{0,s} \approx 0.12$  (0.08) at



1 Gyr;  $f_{0,s} \approx 0.10$  (0.07) at 10 Gyr (Kenyon & Bromley 2008, 2010). For the very strong planetesimals considered here,  $f_{0,vs} \approx 0.26$  (0.16) at 1 Gyr (10 Gyr). Thus, the cascade removes 74% to 93% of the initial mass at 30 AU on 1–10 Gyr timescales.

The amount of solid material remaining in the disk depends on the initial maximum size of the planetesimals. In calculations with  $r_0 = 10$  km, the cascade removes roughly a factor of two less mass over 1–10 Gyr. When  $r_0 = 100$  km, the cascade typically removes a factor of 7–8 less mass. Effective cascades require small planetesimals (Kenyon & Bromley 2010). Ineffective cascades leave more mass in the disk and allow more massive planets to form. Thus, the most massive planets grow in ensembles of large and very strong planetesimals (see also Kenyon & Bromley 2008, 2010).

Fig. 2 illustrates the outcomes of growth for an ensemble of 1 km planetesimals in eight annuli at 27–32 AU. Our starting conditions place most of the mass in 1 km planetesimals; the cumulative size distribution of planetesimals is nearly flat. During orderly growth,  $\sim 10^4$  planetesimals reach radii of nearly 10 km in 3 Myr. Once runaway growth begins, a handful of planetesimals grow as large as 100 km. In both cases, the size distribution follows a shallow power law at small radii and an exponential at large radii (e.g., Davis et al. 1999; Kenyon & Luu 1999b). As the evolution makes the transition from runaway to oligarchic growth, the largest objects grow from  $\sim 100$  km (10 Myr) to  $\sim 500$  km (30 Myr) to  $\sim 2000$  km (300 Myr). Because the oligarchs grow faster than smaller planetesimals, the size distribution becomes a fairly smooth power law from  $\sim 10$  km to  $\sim 2000$  km (e.g., Kenyon & Bromley 2004c; Fraser 2009; Schlichting & Sari 2011).

At small sizes ( $r \lesssim 10$  km), the collisional cascade produces inflection points in the size distribution (Kenyon & Bromley 2004c; Pan & Sari 2005; Benavidez & Campo Bagatin 2009; Fraser 2009). Initially, the cascade ‘erodes’ planetesimals with  $r \lesssim 1$  km. Smaller planetesimals erode more than large planetesimals. These planetesimals grow smaller with time. Because the cascade removes smaller planetesimals from an annulus more rapidly than larger planetesimals, the size distribution becomes shallower, creating an inflection point where erosion dominates growth. Eventually, larger collision velocities cause small planetesimals to shatter completely on impact. This process creates another inflection point where shattering dominates erosion. At the smallest sizes, debris from collisions of larger planetesimals dominates shattering, resulting in a sharp rise in the size distribution (e.g., Kenyon & Bromley 2004c, 2005; Pan & Sari 2005; Fraser 2009).

To analyze the time-evolution of the size distribution for a variety of initial conditions, we perform a series of least-squares fits to the results of our calculations (Fig. 3). For each output size distribution at time  $t_i$ , we construct cumulative size distributions  $n_c(r)$  for sets of eight annuli centered at distances  $a_j$  from the central star. With  $N = 64$  annuli in

our calculations, we have eight cumulative size distributions at each timestep. We adopt a cumulative size distribution in the form of a power law  $n_c \propto r^{-q}$  and derive the best-fitting exponents for planetesimals with radii  $r = 0.1\text{--}1$  km ( $q_1$ ),  $r = 1\text{--}10$  km ( $q_2$ ),  $r = 10\text{--}100$  km ( $q_3$ ), and  $r \geq 100$  km ( $q_4$ ). To minimize fluctuations due to Poisson statistics, we restrict these fits to bins with  $n_c(r) \geq 10$ .

Although we could fit the size distribution for  $r \gtrsim 1$  km to the product of a power law and an exponential (e.g., Wetherill 1990; Tanaka & Nakazawa 1994; Lee 2000), several factors influence our choice of piece-wise fits to the overall size distribution. In our calculations, we set the initial maximum sizes of planetesimals at  $r_0 = 1, 10,$  and  $100$  km. Measuring slopes between these sizes allows us to understand how our choices impact our results. Mergers and destructive collisions often produce multiple inflection points in the size distribution (e.g., Kenyon & Bromley 2004c; Fraser 2009). Fitting several distinct power laws allows us to identify the inflection points easily and to compare power laws at sizes smaller and larger than the inflection points. Observations of TNOs are often well-fit by double power laws with a ‘break’ at  $r \approx 10\text{--}100$  km (e.g., Fuentes & Holman 2008; Fuentes et al. 2009; Fraser & Kavelaars 2009; Fraser et al. 2010; Sheppard & Trujillo 2010). Our  $q_3$  and  $q_4$  exponents allow us to compare calculations directly to observations in the outer solar system.

In the next sections, we consider the time-evolution of the four power law exponents and the size of the largest object in an annulus  $r_{max}$ . In every annulus, the growth of planetesimals follows a similar path from orderly growth to runaway growth to oligarchic growth and the collisional cascade. Thus,  $r_{max}$  serves as a proxy for the evolution time  $t$  and allows us to compare results in different annuli at similar evolutionary states (e.g., Kenyon & Bromley 2008, 2010). We begin with a discussion of the evolution of the size distribution at large sizes (§3.1) and then describe the evolution at smaller sizes in subsequent subsections.

### 3.1. The Size Distribution of Large Objects

Fig. 4 illustrates the time evolution of  $r_{max}$  for the calculation described in Fig. 2. In each annulus, the largest objects first grow slowly;  $r_{max}$  grows roughly linearly with time. Once runaway growth begins, large objects grow exponentially;  $r_{max}$  reaches  $\sim 1000$  km in 3 Myr at 15–18 AU, 20 Myr at 22–27 AU, 50 Myr at 33–40 AU, and 200 Myr at 48–58 AU. After planets achieve these radii, the collisional cascade removes small planetesimals more rapidly than planets accrete them. Thus, planets grow much more slowly. Despite the different timescales, planets in all annuli reach the same maximum size of roughly 3000 km.

Fig. 5 shows how  $q_4$  evolves with time. When the first objects with  $r > 100$  km form,

there are many 100 km objects and only a few with larger sizes. Thus, the size distribution at large sizes is very steep and  $q_4$  is large. As the evolution proceeds, runaway growth produces more and more large objects from the ensemble of 100 km objects. With more objects at  $r > 500$  km and fewer at 100 km, the power-law size distribution grows shallower and shallower (Fig. 2);  $q_4$  decreases. In the late stages of oligarchic growth, planets reach their maximum radius. Because large objects mostly accrete material from much smaller objects, the slope then converges on a characteristic value  $q_4 \approx 3$  (Goldreich et al. 2004; Schlichting & Sari 2011). Although the growth of the largest objects is monotonic in time (Fig. 4), small number statistics produces the fluctuations around the steady decrease of  $q_4$  with time shown in the Figure.

To examine the relationship between  $r_{max}$  and  $q_4$ , we consider calculations for each set of initial conditions  $(x_m, r_0, q_{init}, f_i)$ . For each set of calculations, we collect all pairs  $(r_{max}, q_4)$  in all annuli at all times. We then bin these data in increments of 0.1 in  $\log r_{max}$  and calculate the median  $q_4$  in each  $r_{max}$  bin. This procedure yields the variation of median  $q_4$  as a function of  $r_{max}$  and the initial conditions. This median provides a good representation of the typical slope: the inter-quartile range is roughly 2 when  $r_{max}$  is small ( $\sim 100$  km) and roughly 0.5–1.0 when  $r_{max}$  is large ( $\gtrsim 1000$  km).

Fig. 6 shows results for the complete set of calculations at  $a = 15$ –75 AU with  $r_0 = 1$  km and the  $f_w$  fragmentation parameters. For the ensemble of massive disks with  $x_m = 3$  (violet points in the Figure), the median slope is large,  $q_4 \approx 10$ , when  $r_{max} \approx 100$ –300 km. For  $r_{max} \approx 200$ –2000 km, the median  $q_4$  declines roughly monotonically with increasing  $r_{max}$ . As  $r_{max}$  grows from  $\sim 2000$  km to  $\sim 5000$  km, the median  $q_4$  is roughly constant.

The variation of  $q_4$  with  $r_{max}$  is sensitive to the initial disk mass. As the initial disk mass declines from  $x_m = 3$  to  $x_m = 0.01$ , growth times are longer and longer. Due to the impact of gas drag and long-range stirring, small planetesimals in lower mass disks tend to have larger eccentricities at the onset of runaway growth than those in higher mass disks. Larger eccentricities reduce gravitational focusing factors, slowing growth and enabling stirring to grow faster. Because slower growth is more orderly, large objects have shallower size distributions. When  $r_{max} \approx 100$ –300 km, lower mass disks thus have a smaller median  $q_4$  than higher mass disks. Because growth is very slow for the smallest disk masses, all calculations with  $x_m \lesssim 0.1$  have roughly the same median  $q_4 \approx 4$ .

For disks with  $x_m \gtrsim 0.3$ , gas drag (long-range stirring) is more (less) effective. With larger gravitational focusing factors in more massive disks, growth is relatively fast. Once a few 100 km objects form, a stronger runaway leads to a more pronounced decline of  $q_4$  with  $r_{max}$ . As  $r_{max}$  increases from roughly 100 km to  $\sim 2000$  km, the median  $q_4$  declines roughly linearly with  $r_{max}$ . Once  $r_{max} \gtrsim 2000$  km, the median  $q_4$  is roughly constant. In lower mass

disks, the median  $q_4$  declines more slowly with increasing  $r_{max}$ . Because low mass disks never produce objects with  $r_{max} \gtrsim 2000$  km, the median  $q_4$  is never constant with increasing  $r_{max}$ .

In addition to the clear dependence on  $x_m$ , the median  $q_4$  is also sensitive to the initial maximum planetesimal size  $r_0$  (Fig. 7). For  $r_{max} \approx 100$ –300 km and  $x_m \approx 1$ –3, the median  $q_4$  steadily increases with larger  $r_0$ , from  $q_4 \approx 8$ –9 for  $r_0 = 1$  km to  $q_4 \approx 10$ –11 for  $r_0 = 10$  km to  $q_4 \approx 13$  for  $r_0 = 100$  km. Independent of  $r_0$ , the median  $q_4$  declines steadily with larger  $r_{max}$ . At the largest  $r_{max}$  attained in our calculations, the median  $q_4$  converges on an equilibrium slope  $\sim 3$ –4. Calculations with smaller  $r_0$  yield smaller values for this equilibrium slope.

The behavior of the  $q_4$ – $r_{max}$  relation is remarkably independent of semimajor axis (Table 2, Fig. 8). In calculations at 30–150 AU, our 10 Gyr evolution times yield larger  $r_{max}$  than the 1 Gyr evolution times for calculations at 15–75 AU. Otherwise, the median slope at small  $r_{max}$ , the monotonic decline in slope at  $r_{max} \approx 300$ –2000 km, and the roughly constant slope for  $r_{max} \gtrsim 2000$  km closely follow the relations established at 15–75 AU. Our results show some indication for a smaller inter-quartile range in the median  $q_4$  at larger semimajor axis. Confirming this trend requires a larger ensemble of calculations.

Despite the insensitivity to semimajor axis, the median slope depends strongly on the initial size distribution (Table 2, Fig. 9). In calculations where the initial mass is distributed among planetesimals with sizes of 1 m to 1 km, the median  $q_4$  is systematically smaller ( $\sim 1$ –2) throughout the evolution. This behavior is independent of  $r_0$ . All of these calculations begin with a substantial amount of mass in objects with sizes of 0.1 km or smaller. During runaway growth, collisional grinding removes some of this material from the grid. Compared to calculations where all of the initial mass is concentrated in the largest planetesimals, the largest objects in these calculations accrete material from a lower mass reservoir of small planetesimals which are easier to erode. Thus, the growth of the large objects is relatively slower and the median slope is smaller. Because calculations with larger  $r_0$  have a smaller fraction of the initial mass in small planetesimals, this difference is smaller in calculations with larger  $r_0$ .

To conclude this discussion, Fig. 10 shows how the  $q_4$ – $r_{max}$  relation depends on the fragmentation parameters. For all  $x_m$ , larger planets grow in disks composed of stronger planetesimals. Once the collisional cascade begins, collisions remove more mass from weak planetesimals than from strong planetesimals. At identical evolution times, disks composed of weak planetesimals therefore have less mass in bins with small planetesimals. With oligarchs accreting most of their mass from small planetesimals, they do not grow as rapidly or as large when planetesimals are weak.

Despite the differences in  $r_{max}$ , the median  $q_4$  is fairly independent of the fragmentation parameters (Table 2). In the most massive disks with  $x_m = 0.33$ –3, calculations with stronger planetesimals have slightly larger  $q_4$  than calculations with weak planetesimals:  $q_4 = 2.9$ –4.1 for  $f_w$ ,  $q_4 = 3.2$ –4.3 for  $f_s$ , and  $q_4 = 3.1$ –4.2 for  $f_{vs}$ . These differences are smaller than the typical inter-quartile range of 0.5–1.0 when  $r_{max} \approx 1000$  km. In lower mass disks with  $x_m \lesssim 0.1$ , calculations with stronger planetesimals tend to have shallower slopes, but the inter-quartile ranges are still much larger than the differences.

To summarize, Figs. 6–10 demonstrate a clear relation between the size of the largest object and the slope of the cumulative size distribution for  $r \gtrsim 100$  km. For a broad range of initial conditions and fragmentation parameters,  $q_4$  is large (6–12) when  $r_{max} \approx 300$ –500 km and small (2–5) when  $r_{max} \approx 1000$ –3000 km. For any  $r_{max}$ , disks with smaller masses have smaller  $q_4$  than more massive disks.

To understand how the the rest of the size distribution evolves with  $r_{max}$ , we now consider the other three power-law exponents. We begin with the size distribution of 0.1–1 km objects in §3.2 and then discuss the evolution of 1–10 km (10–100 km) objects in §3.3 (§3.4).

### 3.2. The Size Distribution of 0.1–1 km Objects

The slope of the cumulative size distribution for 0.1–1 km objects,  $q_1$ , is a proxy for the evolution of objects smaller than  $r_0$ . As the largest objects grow, they remove planetesimals from this size range. During runaway growth and the early stages of oligarchic growth, oligarchs accrete only a small fraction of the mass in 0.1–1 km objects (KB08, KB10). Thus, the slope of this size distribution ( $q_1$ ) should remain roughly constant with increasing  $r_{max}$ . Once the collisional cascade begins, destructive collisions among small objects remove material from this range of sizes; destructive collisions among larger objects add material. Although the evolution of the slope then depends on the relative importance of destructive collisions among large and small objects, the collisional cascade eventually removes all of the mass in 0.1–1 km objects from every annulus (KB08, KB10). Thus,  $q_1$  should evolve dramatically during the cascade.

Fig. 11 shows the variation of the median  $q_1$  with  $r_{max}$  for all calculations with the  $f_w$  fragmentation parameters. Each panel illustrates results for a different value of  $r_0$ ; the lower (upper) set of points corresponds to calculations with initial  $n_c \propto r^{-0.5}$  ( $n_c \propto r^{-3}$ ). Colors indicate initial disk mass ranging from  $x_m = 3$  (violet) to  $x_m = 0.01$  (maroon) as in Fig. 6. The remarkable overlap of colored points demonstrates that the evolution of the median  $q_1$

is independent of initial disk mass.

For calculations with  $r_0 = 1$  km, there are two main features of the evolution of  $q_1$  with  $r_{max}$ . As long as  $r_{max} \lesssim 300$ –500 km,  $q_1$  is constant. In the lower panel of Fig. 11,  $q_1$  remains fixed at its initial value as the largest objects grow from sizes of a few km up to roughly 300 km. Thus, the size distribution of 0.1–1 km objects ‘remembers’ the initial size distribution throughout runaway and oligarchic growth.

Once the collisional cascade begins, the general evolution of  $q_1$  is nearly independent of the initial size distribution and the initial size of the largest planetesimal. As the largest objects grow to sizes of  $\sim 1000$  km, all size distributions begin to converge on  $q_1 \approx 2.0$ –2.5 (Table 3). After maintaining this limit for a small range in  $r_{max}$ ,  $q_1$  approaches a limiting value of 0.0–0.5. As the cascade removes nearly all of the mass from an annulus,  $q_1$  remains at this limiting value.

The intermediate value of  $q_1 \approx 2.0$ –2.5 results from collisional erosion (see the Appendix for a simple derivation). When the cascade begins, the ratio of the collision energy to the binding energy is  $Q_c/Q_D^* \approx 0.1$ –1. In this regime, collisions produce a modest net reduction in the mass of the larger object. Together with the mass of the smaller object, this material is lost as debris and accumulates in much smaller mass bins. Smaller objects are easier to erode. Thus, the size distribution evolves from the growth limit of roughly 3–4 to an intermediate limit of roughly 2.0–2.5.

The final limiting value of  $q_1$  results from complete shattering (see the Appendix). As the cascade continues, the largest objects grow. Collision velocities among the smaller objects also grow. Once  $Q_c/Q_D^* \gtrsim 2$ –3, nearly all of the mass of two colliding objects goes into debris. Within the 0.1–1 km size range, all objects are susceptible to shattering. When shattering of the small objects becomes important,  $q_1$  approaches zero (Kenyon & Bromley 2004c).

For calculations with  $r_0 = 10$ –100 km, 0.1–1 km objects collide and merge into larger objects before the collisional cascade begins. Based on the evolution of the largest objects in Figs. 6–10, growth tends to produce size distributions with  $q \approx 2$ –4. Thus, when the initial size distribution is steep ( $n_c \propto r^{-3}$ ), there is little evolution in  $q_1$  for  $r_{max} \lesssim 300$ –500 km (Fig. 11, upper sets of points in the middle and upper panels). When the initial size distribution is shallow ( $n_c \propto r^{-0.5}$ ), slow growth leads to a gradual evolution from  $q_1 \approx 0$  to  $q_1 \approx 2$ –3 (Fig. 11, lower sets of points in the middle and upper panels).

Aside from this difference in the early evolution of  $q_1$ , these calculations also approach the two limiting values earlier in their evolution (at smaller  $r_{max}$ ). When  $r_0 = 10$ –100 km, there is initially less mass in the 0.1–1 km range; thus, the collisional cascade modifies  $q_1$

earlier. At the onset of the collisional cascade, calculations with  $r_0 = 1$  km have most of their mass in 0.1–1 km planetesimals. Because it takes more collisional debris to change  $q_1$  in these calculations,  $q_1$  begins to change when  $r_{max}$  is larger. In these calculations,  $q_1$  also has a larger dispersion as a function of initial disk mass and  $r_{max}$ .

Analyzing calculations with other fragmentation parameters yields nearly identical results (Table 3). The trend of the evolution is always independent of initial disk mass. For  $r_0 = 1$  km,  $q_1$  always remains close to its initial value. When  $r_0 = 10$ –100 km,  $q_1$  remains roughly constant (when the initial  $q_1$  is larger than 2) or slowly evolves to  $q_1 \approx 2$ –3 (when the initial  $q_1$  is smaller than 2). After the cascade commences,  $q_1$  first evolves to the canonical slope for erosive collisions of 2.0–2.5 (at  $r_{max} \approx 1000$  km) and then to the canonical shattering slope of roughly 0.0–0.5 (at  $r_{max} \approx 3000$ –5000 km). Although it always occurs at  $r_{max} \approx 500$ –1500 km, the transition from the initial  $q_1$  to the canonical  $q_1$  depends on the amount of mass initially in 0.1–1 km objects. Disks with less (more) mass in these objects make the transition at smaller (larger)  $r_{max}$  and earlier (later) in evolution time.

### 3.3. The Size Distribution of 1–10 km Objects

Depending on the initial size of the largest object, the slope of the cumulative size distribution for 1–10 km objects,  $q_2$ , serves two distinct roles. For calculations with  $r_0 = 1$  km, the median  $q_2$  first measures changes in the slope as objects grow to sizes of 10 km and then tracks the changes in the size distribution of these objects throughout the rest of runaway/oligarchic growth and the collisional cascade. In these models, we expect the median  $q_2$  first to decline with increasing  $r_{max}$  (as in the evolution of  $q_4$  with  $r_{max}$ ) and then to evolve to a slope characteristic of the collisional cascade. For calculations with larger objects,  $r_0 = 10$ –100 km, changes in the size distribution for 1–10 km objects should follow the changes in  $q_1$  observed for the 0.1–1 km objects: the median  $q_2$  should evolve slowly to  $\sim 2$ –3 during runaway/oligarchic growth and then evolve more rapidly to a smaller value during the collisional cascade.

Fig. 12 shows the variation of the median  $q_2$  with  $r_{max}$  for all calculations with the  $f_w$  fragmentation parameters. The format is identical to Fig. 11, with separate panels for each  $r_0$ , colors indicating the initial disk mass, and an upper and lower set of points corresponding to our two adopted initial size distributions. As in Fig. 11, the evolution of the median  $q_2$  as a function of  $r_{max}$  is independent of the initial disk mass.

In each panel, the evolution of  $q_2$  follows expectation. In the lower panel ( $r_0 = 1$  km), the median  $q_2$  declines from  $\sim 5$ –6 when  $r_{max} \approx 20$  km to  $\sim 4$  for  $r_{max} \gtrsim 100$  km. This

evolution is independent of the initial size distribution. Once the collisional cascade begins,  $q_2$  declines to  $\sim 2.0$ – $2.5$  as  $r_{max}$  grows from 1000 km to 3000 km. At early times, the slope of the 1–10 km size distribution is similar to the slope of the large object size distribution ( $q_4$ ); at late times, the slope evolves into one of the canonical slopes for the collisional cascade.

For larger  $r_0$ , the evolution of  $q_2$  tracks features of the evolution of  $q_1$ . In the middle panel of Fig. 12,  $q_2$  follows much of the  $q_1$  evolution for 1 km objects (Fig. 11, lower panel). During runaway and oligarchic growth,  $q_2$  remains constant with  $r_{max}$ . Once the cascade begins,  $q_2$  evolves to the canonical value for the early stages of the collisional cascade  $q_2 \approx 2.0$ – $2.5$ . As  $r_{max}$  approaches  $10^4$  km,  $q_2$  remains constant at roughly 2.5 instead of dropping to  $\sim 0$ .

In the upper panel, the evolution of  $q_2$  for  $r_0 = 100$  km similarly tracks the  $q_1$  evolution for  $r_0 = 10$  km. As the largest objects grow from  $\sim 100$  km to  $\sim 1000$  km, 1–10 km objects collide and merge into larger objects. Growth tends to evolve the slope to 2–4. For calculations with  $n_c \propto r^{-3}$  (upper set of points),  $q_2$  does not change. When the initial size distribution is concentrated into large objects ( $n_c \propto r^{-0.5}$ ),  $q_2$  slowly approaches 2. Eventually, the collisional cascade begins;  $q_2$  evolves to 2–2.5 and remains in this range as  $r_{max}$  reaches roughly  $10^4$  km.

The ratio of the collision energy  $Q_c$  to the binding energy  $Q_D^*$  allows us to understand the difference between the  $q_1$  evolution for  $r_0 = 1$  km and the  $q_2$  evolution for  $r_0 = 10$ – $100$  km. When the collisional cascade begins, erosive collisions remove mass from the 0.1–1 km and the 1–10 km size ranges. During this evolution, both  $q_1$  and  $q_2$  evolve to 2.0–2.5. Once  $3000 \text{ km} \lesssim r_{max} \lesssim 10^4 \text{ km}$ , collisions among smaller planetesimals produce shattering. However, the larger planetesimals remain in the erosive regime. As a result, objects are completely removed from the ensemble of 0.1–1 km objects (producing  $q_1 = 0.0$ – $0.5$ ) and slowly eroded among the ensemble of 1–10 km objects (leaving  $q_2$  at 2.0–2.5).

Results for calculations with the  $f_s$  and  $f_{vs}$  fragmentation parameters are nearly identical to those with the  $f_w$  fragmentation parameters. When collisions produce mergers instead of debris,  $q_2$  evolves from its initial value to the canonical ‘merger’ limit of 2–4. When  $r_0$  is 1 km,  $q_2$  has no memory of the initial size distribution. Calculations with larger  $r_0$  remember the initial  $q_2$  and maintain this slope throughout much of the evolution. Once the cascade begins,  $q_2$  always evolves to  $\sim 2$ . Because 1–10 km objects are not completely shattered at any point in the collisional cascade,  $q_2$  always remains larger than  $\sim 2$  and never drops to 0–1.



### 3.4. The Size Distribution of 10–100 km Objects

Based on our results for  $q_1$  and  $q_2$ , the evolution of  $q_3$ , the slope for 10–100 km objects, should follow one of two paths. When the initial size of the largest planetesimal is 10 km or smaller, planetesimals must grow to fill the 10–100 km size bins. Growth produces a characteristic evolution of the slope from large values to  $\sim 2$ –4 (Fig. 6). As the evolution makes the transition from growth to the collisional cascade, the slope evolves to a canonical value of roughly 2. Because 10–100 km objects are harder to shatter than 1–10 km objects, the slope produced by the cascade should never fall below 2. When planetesimals have initial sizes larger than 10 km, collisional growth requires a long time to erase the initial size distribution. Eventually, growth and the cascade modify the size distribution, which should approach the canonical value of 2.

Fig. 13 confirms these expectations for calculations with the  $f_w$  fragmentation parameters. Following the format of Figs. 11–12, there is a panel for each  $r_0$ , colors indicating the range in  $x_m$ , and sets of points for each initial size distribution. Once again, the evolution is nearly independent of the initial disk mass.

For calculations with  $r_0 = 1$  km, growth initially produces large  $q_3 \approx 4$ –6. Shallower initial size distributions and more massive disks tend to yield larger  $q_3$ . As objects grow, all calculations converge on a smaller range of  $q_3$ ,  $\sim 2.5$ –3.5, with smaller initial disk masses favoring smaller  $q_3$ . For  $r_{max} \gtrsim 1000$ –2000 km,  $q_3$  is independent of initial disk mass.

When  $r_0 = 10$  km, growth leads to a smaller range of initial median slopes,  $q_3 \approx 5$ –6 for  $r_{max} \approx 200$  km. These median slopes are independent of the initial size distribution and the initial disk mass. As the largest objects grow to  $r_{max} \approx 1000$  km,  $q_3$  reaches an approximate equilibrium at  $\sim 4$ . Once the cascade begins, this slope gradually declines to  $q_3 \approx 2$ .

This evolution for  $q_3$  follows the evolution of  $q_2$  for calculations with  $r_0 = 1$  km. Independent of the initial size distribution, growth produces a characteristic size distribution which slowly evolves to shallower slopes as the largest objects grow. Eventually, the cascade changes the size distribution and the median  $q_3$  becomes smaller. In the middle panel of Fig. 13, this change occurs when  $r_{max} \gtrsim 3000$  km. A similar, but less obvious, change in slope occurs for the  $r_0 = 1$  km calculations in the lower panel.

When  $r_0 = 100$  km,  $q_3$  remembers the initial size distribution throughout most of the evolution (Fig. 13, upper panel). In these calculations, the initial size distribution is unaffected by runaway/oligarchic growth and the early stages of the collisional cascade. Throughout these phases of the evolution, growth is slow and collisions have little impact on large objects. Thus, the size distribution is unchanged. During the late stages of the cascade, occasional collisions among large objects produce some debris which fills all mass bins in the 10–100 km

size range. Independent of the initial size distribution, this debris drives the slope of the size distribution to the canonical value of  $q_3 = 2.0\text{--}2.5$ .

The evolution of  $q_3$  is independent of the fragmentation parameters (Table 3). When the planetesimals are initially small,  $q_3$  first evolves from large values ( $\sim 4\text{--}6$ ) to small values ( $\sim 3$ ). Once the cascade begins,  $q_3$  evolves to  $2.0\text{--}2.5$ . In this size range, the collisional cascade has less impact than at smaller sizes. Thus, the transition from the  $q_3 \approx 3\text{--}4$  characteristic of runaway/oligarchic growth to  $q_3 \approx 2.0\text{--}2.5$  occurs at larger  $r_{max}$  (and later evolution time).

### 3.5. Summary of Size Distribution Evolution

At 15–150 AU, the evolution of planetesimals follows a similar path at every distance from the central star. Initially, collisional damping and gas drag reduce the velocities of small objects. Among larger objects, low velocity collisions produce mergers instead of debris. Along with dynamical friction and viscous stirring, damping produces large gravitational focusing factors; this evolution leads to runaway growth of the largest planetesimals. As these protoplanets grow, they stir up the leftover smaller planetesimals. Eventually, collisions among the leftovers produce debris instead of mergers. A collisional cascade ensues, which grinds planetesimals with sizes of 1–3 km and smaller to dust.

Despite the similarity in the evolutionary path, there is considerable diversity in the overall outcome. For identical starting conditions, the stochastic nature of coagulation leads to a broad range in the rate protoplanets grow, in the maximum radius of protoplanets, in the distribution of sizes as a function of time, and in the amount of mass lost through the collisional cascade. Although this diversity does not mask clear trends in the median outcome as a function of initial conditions (Kenyon & Bromley 2008, 2010), the chaotic nature of the evolution prevents associating a single outcome with a single set of starting conditions.

To quantify the overall evolution of the size distribution of icy planetesimals at 15–150 AU, we define four slopes,  $q_1\text{--}q_4$ , which measure the best-fitting slope of a power-law size distribution between 0.1–1 km ( $q_1$ ), 1–10 km ( $q_2$ ), 10–100 km ( $q_3$ ), and 100 km to  $r_{max}$  ( $q_4$ ). For all  $r_{max} \gtrsim 200$  km, we derive the median slopes and the inter-quartile range as a function of  $r_{max}$ . We use median  $q_1\text{--}q_4$  and the inter-quartile range to track the evolution of the size distribution and to measure the range of outcomes as a function of initial conditions.

Based on these slopes, we infer several general features of the evolution:

- For all distances from the central star, the growth of icy planets leads to size distributions with  $q \approx 2\text{--}4$  (see also Kenyon & Luu 1999b; Kenyon 2002; Goldreich et al. 2004;

Schlichting & Sari 2011). This size distribution results from large objects accreting primarily small objects rather than other large objects. As largest objects grow, the slope evolves from  $q_4 \approx 6\text{--}14$  when  $r_{max} \approx 200$  km to  $q_4 \approx 2\text{--}4$  when  $r_{max} \gtrsim 1000$  km.

- The collisional cascade produces shallower slopes in the size distribution,  $q \lesssim 2.0\text{--}2.5$ . During the cascade, several processes set the size distribution for objects with  $r \gtrsim 0.1$  km (see also O’Brien & Greenberg 2003; Kenyon & Bromley 2004c; O’Brien et al. 2005; Pan & Sari 2005): (i) growth by mergers ( $q \approx 3$ ), (ii) debris production ( $q \approx 2.5\text{--}3$ , e.g., Dohnanyi 1969; O’Brien & Greenberg 2003), (iii) erosion ( $q \approx 2.0\text{--}2.5$ ; see the Appendix) and (iv) shattering ( $q \approx 0.0\text{--}0.5$ , e.g., Kenyon & Bromley 2004c, and the Appendix). At the smallest sizes ( $r \lesssim 0.01\text{--}0.1$  km), debris production dominates the size distribution and  $q \approx 3.5\text{--}4$  (O’Brien & Greenberg 2003; Kenyon & Bromley 2004c, 2005; O’Brien et al. 2005; Krivov et al. 2005; Kenyon & Bromley 2008; Benavidez & Campo Bagatin 2009; Fraser 2009; Kenyon & Bromley 2010). At larger sizes, erosion slowly removes mass from all objects and produces  $q \approx 2.0\text{--}2.5$ . Once the collisional cascade reaches its peak ( $r_{max} \gtrsim 3000$  km), shattering of 0.1–1 km objects leads to  $q \approx 0.0\text{--}1.0$ .
- The evolution of the large object size distribution is independent of radial distance from the central star and is generally independent of the fragmentation parameters. However, the evolution of  $q_4$  is sensitive to the initial size of the largest planetesimal ( $r_0$ ) and the initial mass of the disk ( $x_m$ ). Lower mass disks evolve over a smaller range of  $q_4$ . Calculations with larger planetesimals tend to produce larger median  $q_4$ .
- For any  $r_{max}$ , the range in  $q_4$  is fairly large. At small sizes ( $r_{max} \approx 200\text{--}500$  km), the inter-quartile range about the median  $q_4$  is roughly 2. This range drops to roughly 1 at  $r_{max} \gtrsim 1000$  km. For a typical  $q_4 \approx 3$ , roughly 50% of calculations with the same initial conditions yield  $q_4 = 2.5\text{--}3.5$ . The rest have  $q_4 = 2\text{--}2.5$  and  $q_4 = 3.5\text{--}5$ .
- Among the intermediate mass objects with  $r = 1\text{--}100$  km, the evolution of the slope of the size distribution depends on the initial size of the largest planetesimal.
- When  $r_0$  is small, growth produces objects with  $r = 1\text{--}100$  km. Growth erases knowledge of the initial size distribution; the slope evolves to the standard ‘growth slope,’  $q_2 \approx q_3 \approx 2\text{--}4$ . Once the collisional cascade begins, the slopes evolve to the canonical value of 2 for erosive collisions.
- When  $r_0$  is large, growth cannot change the initial slope of the size distribution. Thus,  $q_2$  and  $q_3$  remember the initial  $q$  until the onset of the collisional cascade. Once the cascade begins, erosive collisions lead to  $q_2 \approx q_3 \approx 2.0\text{--}2.5$ .

## 4. APPLICATION TO THE TRANSNEPTUNIAN REGION

To apply these results to the formation of TNOs, we place our calculations in the context of recent observations of TNOs and models for the formation of the solar system. The observations allow us to set  $r_{max}$  and the slopes of the size distribution in various size ranges. Observations of young stars in nearby star-forming regions and theories of solar system formation constrain the initial properties of the protosolar disk and the likely epoch(s) of TNO formation. We begin with the theoretical issues and then summarize the direct observational constraints.

### 4.1. Theoretical Constraints

Current theories for the origin of the solar system broadly explain the nature of TNOs as a several step process. During the early evolution of the protosolar disk, dust grains within the disk grow into icy planetesimals (e.g., Weidenschilling 2006; Chiang & Youdin 2010) and then into icy protoplanets (e.g., Lissauer 1987; Kenyon & Luu 1999a; Kenyon & Bromley 2008, 2010). Four protoplanets become gas giants (Pollack et al. 1996; Alibert et al. 2005; Ida & Lin 2008; Lissauer et al. 2009; Bromley & Kenyon 2011a). Sometime after the gas giants reach roughly their final masses, dynamical interactions among the gas giants, the much less massive icy protoplanets, and any leftover planetesimals result in the ejection or migration of icy objects into the transneptunian region and the Oort Cloud (e.g., Malhotra 1993; Hahn & Malhotra 1999; Morbidelli et al. 2004; Tsiganis et al. 2005; Gomes et al. 2005). Once dynamical evolution begins, lower surface densities and larger orbital velocities among the TNOs reduce growth rates and promote collisional erosion (e.g., Stern & Colwell 1997b; Kenyon & Luu 1999a; Kenyon & Bromley 2004c; O’Brien et al. 2005; Kenyon & Bromley 2008; Fraser 2009; Kenyon & Bromley 2010). Thus, dynamical evolution ends the growth of TNOs.

Despite the uncertainty in the theory, this picture constrains the initial mass of the protosolar disk and the likely range of formation times for TNOs. The protosolar disk probably has properties similar to the disks observed in nearby star-forming regions such as Ophiuchus, Orion, and Taurus-Auriga (e.g., Williams & Cieza 2011). Infrared and radio observations demonstrate that these systems lose their gas and dust on timescales of 1–10 Myr (Haisch et al. 2001; Currie et al. 2009; Kennedy & Kenyon 2009; Williams & Cieza 2011). For the solar system, these data constrain the initial disk mass, 0.001–0.1  $M_{\odot}$ , and the timescale, 1–10 Myr, for the formation of gas giant planets.

Dynamical calculations of the solar system place additional limits on the initial disk

mass and the formation time. Several results suggest some TNOs formed at 20–25 AU and then migrated outwards with the giant planets (e.g., Malhotra 1993, 1995; Hahn & Malhotra 1999; Levison & Morbidelli 2003; Morbidelli et al. 2008). To explain the orbital architecture of the giant planets, the TNOs, and the Oort cloud, these calculations rely on a massive disk of solids with  $x_m \gtrsim 1$  at 15–30 AU (Hahn & Malhotra 1999; Levison & Morbidelli 2003; Morbidelli et al. 2008). Although these calculations place little direct constraint on the formation time, Figs. 6–10 demonstrate that more massive disks have larger  $q_4$  at fixed  $r_{max}$ . Thus, relying on a massive disk to enable outward migration places indirect constraints on any combination of formation time,  $r_{max}$ , and  $q_4$ .

Various lines of evidence associate migrating gas giant planets with an increased rate of cratering during the Late Heavy Bombardment (hereafter LHB; e.g., Levison et al. 2001; Gomes et al. 2005; Strom et al. 2005). Although constraints on the cratering history prior to this epoch are weak (e.g., Chapman et al. 2007), detailed analyses suggest the intense period of bombardment ended  $\sim 500$ – $700$  Myr after the formation of the solar system (e.g., Tera et al. 1974; Hartmann et al. 2000; Stöffler & Ryder 2001). It is unlikely that the gas giants migrated after the LHB. Thus, the end of the LHB sets an upper limit on the formation time for TNOs.

For our analysis, we concentrate on the formation of TNOs before the gas giants dynamically rearrange the solar system. The initial conditions chosen for our calculations broadly match the range of initial disk masses and semimajor axes applicable to TNO formation. By following the evolution of TNOs for 1–10 Gyr, we cover the most likely range of formation times,  $\sim 10$ – $700$  Myr. Thus, our calculations can provide clear tests of the coagulation picture for TNO formation.

## 4.2. Observational Constraints

Recent observations place excellent limits on the masses and radii of the largest TNOs. All of the major dynamical classes (e.g., Gladman et al. 2008) have at least one large object with radius  $r \approx 450$ – $1300$  km (e.g., Sheppard et al. 2011; Petit et al. 2011). All-sky surveys are now nearly complete to an R-band magnitude  $R \approx 21$ , the approximate brightness of an object with radius  $r \approx 350$  km and an albedo of 10% at 42 AU (e.g., Schwamb et al. 2010; Sheppard et al. 2011). Thus, the sample of largest TNOs is probably complete at 40–50 AU. For large TNOs with binary companions, period measurements yield reliable masses of roughly  $1.5 \times 10^{24}$  g for Quaoar (Fraser & Brown 2010) to roughly  $1.5 \times 10^{25}$  g for Pluto (Buie et al. 2006) and  $1.6 \times 10^{25}$  g for Eris (Brown & Schaller 2007). In our calculations, this mass range corresponds to  $r \approx 600$ – $1400$  km. Thus, a typical  $r_{max} = 1000 \pm 400$  km matches

the current population of the largest TNOs.

For deep surveys with sufficient observations, the luminosity function – written as  $\sigma(m)$ , the surface number density of objects brighter than magnitude  $m$  – is reasonably well-fit by a double power-law,

$$\sigma(m) = \sigma_{m_0} \frac{1 + 10^{(\alpha_L - \alpha_S)(m_{eq} - m_0)}}{10^{\alpha_L(m - m_0)} + 10^{(\alpha_L - \alpha_S)(m_{eq} - m_0) - \alpha_S(m - m_0)}} \quad (9)$$

where  $\sigma_{m_0}$  is a normalization factor,  $m_0$  is a reference magnitude,  $m_{eq}$  is the brightness where the two power laws merge,  $\alpha_L$  is the slope of the size distribution at large sizes, and  $\alpha_S$  is the slope of the size distribution at small sizes (e.g., Petit et al. 2006, 2008; Fuentes & Holman 2008; Fuentes et al. 2009; Fraser et al. 2008; Fraser & Kavelaars 2009; Fraser et al. 2010; Schwamb et al. 2010; Sheppard et al. 2011; Petit et al. 2011).

Converting observations of the surface number density to constraints on the size distribution requires additional information (e.g., Fraser et al. 2008; Petit et al. 2008). If the cumulative size distribution and the distribution of albedos follow power laws with exponents  $q$  (for the size distribution) and  $\beta$  (for the albedo),

$$q = 5(\alpha - \beta/2) + 1. \quad (10)$$

Although TNOs display a broad range of albedos (e.g., Stansberry et al. 2008; Brucker et al. 2009), current data suggest a roughly constant albedo of 2%–20% for  $r \approx 30$ –500 km and a larger albedo of 20% to nearly 80% for  $r \gtrsim 700$  km (Fig. 3 of Stansberry et al. 2008). Most objects comprising the luminosity function are faint; adopting  $\beta \approx 0$  is therefore a reasonable assumption. The slope of the size distribution is then  $q = 5\alpha + 1$ .

Recent analyses indicate a range in the slope of the luminosity function at large sizes. Several deep surveys yield  $\alpha_L \approx 0.70$ –0.76, implying  $q_L \approx 4.5$ –4.8 for  $\beta = 0$  (Fuentes & Holman 2008; Fuentes et al. 2009; Fraser & Kavelaars 2009). Fraser et al. (2010) divided their sample of the classical Kuiper belt into a set of cold objects with inclination  $i \leq 5^\circ$  and a set of hot objects with  $i \geq 5^\circ$ . Their results suggest  $\alpha_L \approx 0.80$  ( $q_L \approx 5$ ) for the cold objects and  $\alpha_L \approx 0.40$  ( $q_L \approx 3$ ) for the hot objects (see also Levison & Stern 2001; Bernstein et al. 2004; Fuentes & Holman 2008; Fuentes et al. 2011). Sheppard et al. (2011) also prefer a shallower slope for the large objects.

Other observations also distinguish the hot and cold populations within the Kuiper belt. The largest cold KBOs are smaller (Levison & Stern 2001) and have a larger fraction of binary companions (Noll et al. 2008) than the largest hot KBOs. The cold KBOs also have larger albedos (Brucker et al. 2009). Although there is no consensus, some results suggest that the cold KBOs are considerably redder than the hot KBOs (e.g., Tegler & Romanishin 2000; Trujillo & Brown 2002; Peixinho et al. 2004; Gulbis et al. 2006; Peixinho et al. 2008).

This diversity suggests that the cold and hot KBOs formed in different locations or have had different collisional histories (Levison & Stern 2001; Malhotra 1993; Gomes 2003; Levison & Morbidelli 2003; Levison et al. 2008). In current dynamical models, the observed  $(a, e, i)$  distributions of the hot KBOs are a result of formation at 15–25 AU and subsequent migration and scattering during the migration of the giant planets. In this picture, the cold population formed at a larger distance, perhaps *in situ* (see Batygin et al. 2011a, and references therein).

To assign  $r_{max}$  for the hot and cold populations, we use results from direct mass estimates of individual KBOs (e.g., Grundy et al. 2009; Fraser & Brown 2010; Grundy et al. 2011) and deep probes of the KBO luminosity function (e.g., Fraser & Kavelaars 2009; Fraser et al. 2010; Petit et al. 2011). These analyses consistently demonstrate that the largest hot KBOs are systematically larger than the largest cold KBOs (see also Levison & Stern 2001). We infer a typical ‘size ratio’  $\gtrsim 1.5$ –2, suggesting  $r_{max} \approx 1000$  km for the hot objects and  $r_{max} \lesssim 600$  km for the cold objects. Although the true  $r_{max}$  for the cold population might be less than 600 km, results for  $(q_4, r_{max}) = (5, 600 \text{ km})$  are a reasonable proxy for any size in the 400–600 km ( $0.4 - 1.3 \times 10^{24}$  g) range. After deriving the constraints these observations place on the models, we will consider alternative models for a smaller  $r_{max} = 100$ –200 km.

### 4.3. Testing the Calculations

To use the observational and theoretical constraints to test our calculations, we assume that our  $q_4$  is equivalent to the observed  $q_L$ . For our purposes, the  $q_4$  derived for the cold KBOs is identical to the  $q_4$  inferred from most deep surveys. Thus, we consider the implications of  $q_4 = 3$  and  $q_4 = 5$  for  $r_{max} = 600$ –1400 km. After a basic application of our models to these data in §4.3.1, we derive a set of ‘success fractions,’ which measure the fraction of models that match the observations of  $q_4$  and  $r_{max}$  (§4.3.2). This analysis yields two plausible models for the formation of the cold and hot TNOs: (i) ensembles of 1 km planetesimals in a massive disk with  $x_m = 0.3$ –3 and (ii) ensembles of 10 km planetesimals in a less massive disk with  $x_m = 0.03$ –0.3. To select the ‘best’ model, we consider the range of formation times at 20–50 AU (§4.3.3). These results favor ensembles of 1 km planetesimals as the most likely starting point for the current populations of hot and cold TNOs.

#### 4.3.1. Basic Tests

The steep size distribution of the cold Kuiper belt objects (KBOs) suggests these objects form in a massive disk. Although many calculations yield  $q_4 \approx 5$  when  $r_{max} = 1000$  km, the median  $q_4$  for low mass disks is usually much smaller than 4 (Table 2). Thus, more massive disks with  $x_m \approx 0.3$ –3 are strongly favored over low mass disks with  $x_m \lesssim 0.3$ . Because the median  $q_4$  also depends on the initial planetesimal size, the initial disk mass required to match the observations depends on  $r_0$ . Larger  $r_0$  favors lower mass disks. For all  $r_0$ , models with  $x_m \approx 0.3$ –3 yield good matches to the observed  $q_4$ .

The shallow size distribution of the hot KBOs allows us to rule out a broader range of collision models. From Figs. 6–10 and Table 2, calculations with 100 km planetesimals never achieve  $q_4 \lesssim 3.5$  when  $r_{max} = 1000$  km. Thus, these models provide a poor match to the size distribution of large, high inclination KBOs. Results for calculations with 10 km planetesimals are a little more encouraging. Although calculations with a single planetesimal size fail, growth in a low mass disk ( $x_m \approx 0.03$ ) with a range of planetesimal sizes yields  $q_4$  close to 3.

For the hot KBOs, a broad range of calculations with 1 km planetesimals result in a good match to the observed  $q_4$  with  $r_{max} = 1000$  km. Models with a range of initial planetesimal sizes have a smaller median  $q_4$  than those with a single initial size; thus, these models provide a better match to the observations. Models with small initial disk masses achieve smaller  $q_4$  than models of massive disks. Current uncertainties in the slope allow a broad range of initial disk masses to match the observations.

#### 4.3.2. Success Fractions

Having established rough limits on the initial disk mass and planetesimal size, we now quantify the range of calculations which match the observational constraints on  $r_{max}$  and  $q_4$ . To make these choices, we consider ensembles of results for each set of initial conditions and fragmentation parameters. From Table 1, there are three ensembles with  $r_0 = 10$  km and 100 km, and five ensembles with  $r_0 = 1$  km. For each of these ensembles, we collect all pairs of  $(r_{max}, q_4)$  and bin these data in increments of 0.1 in  $\log r_{max}$ . Within each  $r_{max}$  bin, stochastic effects produce a broad range of  $q_4$ . Thus, we identify the fraction of calculations within each bin that match an adopted target  $q_4$  as a function of  $r_{max}$ . To span the observed range, we consider two target slopes,  $q_4 = 3 \pm 0.25$  and  $5 \pm 0.25$ , for  $r_{max} = 600$  km, 1000 km, and 1400 km.

To judge the uncertainties of the derived ‘success fractions,’ we examine the variation of



the success fraction as a function of  $r_{max}$ . For a single set of initial conditions ( $x_m, r_0, q_{init}, f_i$ ), the success fraction usually has an obvious trend (from larger to smaller success fraction or from smaller to larger success fraction) as a function of  $r_{max}$ . We set the uncertainty in a single success fraction as the dispersion around this trend. Typically, this dispersion (and thus the adopted uncertainty) is 0.05–0.10.

Fig. 14 shows results for a target  $q_4 = 5 \pm 0.25$ . The three sets of vertical panels plot the fraction of successful models for  $r_{max} = 600$  km (left panels), 1000 km (middle panels), and 1400 km (right panels). The three sets of horizontal panels plot the success fraction for calculations with  $r_0 = 1$  km (lower panels), 10 km (middle panels), and 100 km (upper panels). Within each panel, colored lines show the variation of the success fraction as a function of the initial disk mass. Different colors indicate different initial mass distributions and fragmentation parameters as listed in the figure caption (see also Table 1).

Clearly, a broad range of calculations match the target slope at rates of roughly 20% to 50%. For  $r_0 = 1$  km and  $r_{max} = 600$  km (lower left panel), calculations with any set of initial conditions and low disk masses ( $x_m \lesssim 0.1$ ) fail to match the target slope. Models with larger initial disk masses ( $x_m \gtrsim 0.1$ ) have larger success fractions. Within this range of  $x_m$ , calculations with an initially large range of planetesimal sizes (green, orange, and magenta curves) are more successful than calculations with a single planetesimal size (violet and blue curves). As  $r_{max}$  increases to 1000 km (lower middle panel) and to 1400 km (lower right panel), the success fraction systematically decreases. In these panels, calculations with a single planetesimal size are somewhat more successful than those with a range of planetesimal sizes. Once  $r_{max} = 1400$  km, however, few calculations successfully match the target slope.

Calculations with larger  $r_0$  also match the target slope. For  $r_0 = 10$  km and 100 km, success fractions of 20% to 40% are common. Among the  $r_0 = 10$  km panels, there is a clear trend of larger success fraction with increasing initial disk mass. Although there is a small trend of more success for calculations with a single initial planetesimal size, the trend is much weaker than the trend with  $r_{max}$ . Among the models with  $r_0 = 100$  km, less (more) massive disks yield larger success ratios when  $r_{max}$  is small (large). When  $r_{max}$  is small, calculations with a broad range of initial planetesimal sizes often match the data; results for a single initial planetesimal size rarely match the data. This trend reverses at large  $r_{max}$ , when calculations with a single planetesimal size are often more successful.

Fig. 15 repeats Fig. 14 for a target  $q_4 = 3 \pm 0.25$ . In these examples, calculations with 1 km planetesimals are much more successful than those with large planetesimals. For any  $r_{max}$  (any vertical column of panels in the figure), the success fractions decline monotonically from 20%–40% at  $r_0 = 1$  km to 0% for  $r_0 = 100$  km. Although there is little trend in the

success fraction with  $r_{max}$  for calculations with  $r_0 = 10\text{--}100$  km, there is a modest trend for  $r_0 = 1$  km: smaller  $r_{max}$  requires disks with smaller masses to match the target slope. In all panels for  $r_0 = 1$  km, there is little trend with the initial size distribution of planetesimals or the fragmentation parameters: all of the initial conditions yield success ratios of 20% to 40% for  $x_m = 0.03\text{--}3$ .

To refine these tests, we now include other constraints on the hot and cold populations. In the dynamical models, hot KBOs formed closer to the Sun and then migrated out to their current orbits. In the context of our coagulation models, objects closer to the Sun grow faster (Fig. 4) and produce shallower size distributions (Fig. 5) over the same evolution time. Both of these features of collisional evolution agree with the observations: the hot KBOs are larger and have a shallower size distribution than the cold KBOs.

To find a combination of starting conditions that match the observations, we consider models that match  $(q_4, r_{max}) = (3, 1000 \text{ km})$  for the hot objects and  $(5, 600 \text{ km})$  for the cold objects. Using results in Figs. 14–15, we rule out any models starting with 100 km planetesimals. These calculations never match the shallow slope for the hot objects. However, two options with 1 km and 10 km planetesimals are equally likely:

- 10 km planetesimals in a low mass disk ( $x_m = 0.03\text{--}0.3$ )
- 1 km planetesimals in a massive disk ( $x_m = 0.3\text{--}3$ )

In both cases, models with a single planetesimal size or a range of planetesimal sizes match the constraints reasonably well. Models with a single planetesimal match more often when  $r_0 = 10$  km; models with a range of sizes match more often when  $r_0 = 1$  km.

#### 4.3.3. *The Formation Time*

To select the ‘better’ alternative among these two options, we add a final constraint – the formation time – to our analysis. The dynamical models require TNO formation at 20–40 AU sometime between 1–10 Myr and 500–700 Myr. The smaller of these two constraints is not useful. Only a few models produce TNOs in 10 Myr at 20 AU; none of our calculations produce TNOs in 10 Myr at 40–50 AU. The longer constraint is very useful. Many calculations require more than 1 Gyr to produce 600–1000 km objects at 40–50 AU. Thus, the dynamical models rule out these coagulation models.

To select between the allowed combinations of  $r_0$  and  $x_m$ , we consider the evolution time required to form 1000 km objects as a function of semimajor axis. Fig. 16 shows results

for calculations with the  $f_w$  fragmentation parameters. Results for other calculations are similar. Individual panels plot results for  $r_0 = 1$  km (lower panels),  $r_0 = 10$  km (middle panels), and  $r_0 = 100$  km (upper panels) and two initial size distributions (left and right panels). Colors indicate the initial disk mass, ranging from  $x_m = 3$  (violet) to  $x_m = 0.01$  (maroon) as in Fig. 6.

These results follow standard expectations for coagulation calculations. Formation times always scale with the initial radius of the largest planetesimal (e.g., Lissauer 1987; Kenyon & Luu 1998; Kenyon & Bromley 2010). As  $r_0$  increases from 1 km to 100 km, the clusters of points shift to longer formation times. In a disk with a surface density  $\Sigma \propto x_m a^{-3/2}$ , the formation time scales as  $t_f \propto x_r^{-3} a^3$  (Goldreich et al. 2004; Kenyon & Bromley 2008). As  $a$  increases, formation times in each panel grow rapidly. Similarly, models with smaller  $x_m$  have longer formation times.

The solid horizontal line in each panel indicates the approximate end of the LHB, 500–700 Myr. Applying the additional constraint that TNOs form at  $a \approx 20$ –50 AU yields constraints on all of our calculations:

$$x_m \gtrsim \begin{cases} 0.01 (r_0/1 \text{ km})^{1/2} (a/20 \text{ AU})^3 & \text{all planetesimal sizes,} \\ 0.03 (r_0/1 \text{ km})^{1/2} (a/20 \text{ AU})^3 & \text{one planetesimal size.} \end{cases} \quad (11)$$

When  $r_0 = 100$  km, these constraints are severe: *in situ* formation of TNOs at 40 AU requires  $x_m \gtrsim 1$ –3. Thus, calculations with very large planetesimals are viable only if the initial mass of the disk exceeds the minimum mass solar nebula. For smaller  $r_0$ , calculations with smaller  $x_m$  yield 1000 km TNOs in 500 Myr at 40 AU.

Requiring TNOs to form in 10 Myr places more stringent limits on the initial disk mass and the range of semimajor axes. In this case, TNOs can only form at  $a \approx 20$  AU for massive disks ( $x_m = 1$ –3) composed of 1–10 km planetesimals. Rapid formation times exclude all combinations of models with  $r_0$  larger than 10 km.

These conclusions are independent of the fragmentation parameters. When other initial conditions are held fixed, formation times for icy planets with  $r_{max} \approx 1000$  km are similar for all three sets of fragmentation parameters. Although the size of the largest object varies with  $f_i$  (Fig. 10), the variation of  $q_4$  with  $r_{max}$  is similar for calculations with weak, strong, and very strong planetesimals. Thus, the formation time places strong constraints on the initial disk mass and the initial sizes of planetesimals.

From eq. 11, formation at 40–50 AU places the most severe constraints on the initial disk mass. For 1–10 km planetesimals, we adopt the less restrictive model with all planetesimal

sizes. Then:

$$x_m \gtrsim \begin{cases} 0.1 - 0.2 & 1 \text{ km planetesimals,} \\ 0.3 - 0.6 & 10 \text{ km planetesimals.} \end{cases} \quad (12)$$

Because coagulation models with 10 km planetesimals match the observed range in  $q_4$  and  $r_{max}$  only for  $x_m \approx 0.03$ – $0.3$ , the combined constraints of the formation time, the size of the largest object, and the slope of the large object size distribution strongly favor calculations with 1 km planetesimals.

#### 4.4. Consequences of Small Cold KBOs

Some observations suggest the largest cold KBOs have  $r_{max} \approx 100$ – $200$  km instead of the  $r_{max} = 400$ – $600$  km used in our analysis (e.g., Brucker et al. 2009; Grundy et al. 2009, 2011). To investigate how a smaller  $r_{max}$  impacts our results, we now consider the range of coagulation models which yields an observed  $q = 5 \pm 0.25$  for  $r_{max} = 100$ – $200$  km. For this analysis, we use  $q_3$  as a proxy for the slope of the size distribution for cold KBOs smaller than  $r_{max}$ . For  $r_{max} = 100$ – $200$  km,  $q_4$  provides a poor measure of the slope below 100 km;  $q_3$  provides an accurate measure of the slope over 20–200 km.

To identify coagulation models which match the observed  $q_3$  for a smaller  $r_{max}$ , we derive success fractions for all sets of initial conditions in Table 1 assuming a target  $q_3 = 5 \pm 0.25$  and  $r_{max} = 100$ – $200$  km. For calculations with  $r_0 = 100$  km and  $r_{max} = 100$ – $200$  km,  $q_3$  is identical to the initial slope (see Fig. 13). Because our adopted initial slope is  $q_3 = 0.17$  or 3.0, our calculations never yield the observed  $q_3 = 5$ . Thus, all of our calculations with  $r_0 = 100$  km fail to match the target slope.

Calculations with  $r_0 = 100$  km and a steeper initial size distribution probably cannot match the target slope. When the initial  $q_3 \gtrsim 3$ , most of the mass is in the smallest objects. For modest initial surface densities,  $x_m \gtrsim 0.1$ , growth of these small objects should produce shallower slopes with  $q_3 \approx 3$ – $4$ .

For all other initial conditions, we derive success fractions of 10% to 50%. When  $r_{max}$  is much smaller than 500 km, the collisional cascade has no impact on the slopes of the size distributions. Thus, success fractions for a target  $(q_3, r_{max}) = (5, 100$ – $200 \text{ km})$  are independent of the fragmentation parameters. For calculations with all sizes or one size of planetesimals, there are weak trends of increasing success fractions in more massive disks. Lower mass disks produce slower growth, which tends to yield shallower size distributions. However, this trend is weak for small  $r_{max}$ .

Despite this lack of trends with  $f_i$  or  $x_m$ , there are trends with the initial size and

size distribution of planetesimals. For  $r_0 = 10$  km, a larger fraction of our models match the target  $q_3$  for  $r_{max} = 150$ – $200$  km (40% to 50%) than for  $r_{max} = 100$ – $150$  km (10% to 30%). Calculations with  $r_0 = 1$  km yield smaller success fractions for  $r_{max} = 150$ – $200$  km (10% to 35%) than for  $r_{max} = 100$ – $150$  km (35% to 50%). In both cases, models with a single planetesimal size have somewhat smaller success fractions, but the differences are not significant.

Thus, coagulation models match the observed  $q_3 = 5$  for the cold KBOs when  $r_{max} = 100$ – $200$  km. Calculations with  $r_0 = 1$  km (10 km) yield the target slope more often when  $r_{max} = 100$ – $150$  km (150– $200$  km). With little preference for the disk mass or the fragmentation parameters, this analysis does not identify a clear preference for  $r_0$  or  $x_m$ .

#### 4.5. Summary of Results

The most basic conclusion of our analysis is that the robust relation between  $r_{max}$  and  $q_4$  allows coagulation models to make clear predictions of  $(q_4, r_{max})$  for any deep survey of TNOs. Unambiguous relations between  $q_3$  and  $r_{max}$  also enable clear predictions for small TNOs. In principle, observations of  $(q_4, r_{max})$  or  $(q_3, r_{max})$  can falsify current coagulation models. In practice, current observations agree with the predictions.

Using observational results from deep surveys of TNOs together with conclusions derived from dynamical models of the solar system, we place good constraints on coagulation models for the origin of TNOs throughout the solar system. Fig. 17 summarizes the main results of our analysis. As we add more observational and theoretical constraints to the analysis, the set of coagulation calculations which ‘match’ the constraints narrows. Thus, a complete set of observations for all TNO classes provides a rigorous test of coagulation models.

To summarize current limits on the models, we step through the observational and theoretical constraints. For a single size distribution of TNOs, we derive constraints on coagulation models from  $q_4$  and  $r_{max}$  (top two rows of Fig. 17).

- With a success rate of 20% to 50%, calculations with a broad range of initial conditions and fragmentation parameters can match a target combination  $(q_4, r_{max})$  which is consistent with observations of TNOs.
- For a specific target  $(q_4, r_{max})$ , the range of success rates allows us to rule out some ranges of initial conditions and fragmentation parameters.
- When the target  $(q_4, r_{max}) = (5, 1400 \text{ km})$ , calculations with large planetesimals are more successful than those with small planetesimals (Fig. 14).

- Smaller target slopes,  $q_4 \approx 3$ , appear to rule out calculations with large planetesimals (Fig. 15).
- In all cases, models with large disk masses are more successful than those with small disk masses. Thus, models with massive disks composed of large planetesimals are much more likely to match the target than low mass disks composed of small planetesimals.

Adding in the dynamical constraint that the hot and cold populations originate in different locations of the protosolar disk yields more severe limits on the models. Requiring  $(q_4, r_{max}) = (3, 1000 \text{ km})$  for the hot KBOs and  $(q_4, r_{max}) = (5, 400\text{--}600 \text{ km})$  for the cold KBOs (third row of Fig. 17) leads to these conclusions.

- Models with 100 km planetesimals cannot match the data for any set of initial conditions.
- Models with 10 km planetesimals match the data for low mass disks,  $x_m = 0.03\text{--}0.3$ .
- Models with 1 km planetesimals match the data for massive disks,  $x_m = 0.3\text{--}3$ .

Finally, using the constraint on formation time eliminates models with 10 km planetesimals. Forming TNOs in 500–700 Myr at 20–50 AU requires massive disks with  $x_m = 0.3\text{--}3$  (fourth row of Fig. 17). Thus, we strongly favor models starting with 1 km planetesimals.

Adopting a different observational constraint,  $r_{max} = 100\text{--}200 \text{ km}$ , for the cold KBOs results in similar conclusions. The observed slope for the hot population,  $q_4 = 3$ , drives us to models with small planetesimals in massive disks.

## 4.6. Discussion

Our analysis is the first attempt to apply multiannulus coagulation calculations to modern observations of TNOs. The results indicate that TNOs form within a massive disk composed of small, 1 km planetesimals. This conclusion is similar to recent results on the origin of asteroids, where an initial population of 0.1 km planetesimals seems sufficient to explain the size distribution of asteroids for sizes of 10–100 km (Weidenschilling 2011, for a different conclusion, see Morbidelli et al. 2009). Although we did not consider formation of TNOs from 0.1 km planetesimals, calculations with smaller planetesimals should yield similar results for the size distributions at 10–1000 km. Thus, current data are also consistent with TNO formation from 0.1 km planetesimals.

The similarity of the size distributions for the TNOs and the trojans of Jupiter (Jewitt et al. 2000; Jedicke et al. 2002) and Neptune (Sheppard & Trujillo 2010) suggest a common origin in a massive disk composed of 1–10 km planetesimals (for a discussion of the dynamical origin of these populations, see Morbidelli et al. 2009). Unless the initial surface density of the disk is small ( $x_m \lesssim 0.03\text{--}0.1$ ; see eq. [11]), collisional evolution erases the signatures of many initial conditions on 10–500 Myr timescales. Dynamical models for the orbital architecture require massive disks (Morbidelli et al. 2008). During the dynamical re-arrangement of the giant planets, the large relative velocities among planetesimals leads to a collisional cascade which modifies the size distribution at  $a \approx 15\text{--}30$  AU considerably for  $r \lesssim 100$  km (Figs. 11–13).

The main alternative to this picture is that the observed size distributions for the cold KBOs and the trojans of Jupiter and Neptune are ‘primordial,’ relatively unchanged since the initial process that formed planetesimals from mm-sized or smaller particles (e.g., Sheppard & Trujillo 2010). To evaluate this possibility, we isolate coagulation calculations where an initial size distribution of 100 km and smaller objects produces 110 km or smaller objects prior to the end of LHB. For models with a single size or a range of sizes, calculations with  $x_m \lesssim 0.0003 (a/40 \text{ AU})^3$  satisfy this constraint. Models with larger  $x_m$  yield objects larger than 110 km. For primordial objects formed *in situ* at  $a \approx 20\text{--}30$  AU, this limit implies an initial mass of  $0.003 M_{\oplus}$ , roughly three times larger than the current mass in cold KBOs (e.g., Brucker et al. 2009). Although coagulation models do not directly preclude that cold KBOs and trojans form in a very low mass region of the disk, it seems unlikely that dynamical mechanisms can populate three distinct volumes of the solar system with so little reduction in the total mass (e.g., Morbidelli et al. 2005; Levison et al. 2008; Batygin et al. 2011b; Wolff et al. 2011). Thus, we conclude that the observed size distributions are not primordial.

Comparisons between our calculations and the current size distributions of TNOs make several important assumptions. We assume that the hot and cold populations in the Kuiper belt are representative of all TNOs. Current data do not contradict this assertion (e.g., Sheppard & Trujillo 2010; Petit et al. 2011). Data from ongoing and planned all-sky surveys will eventually yield robust estimates for  $(q_4, r_{max})$  for all dynamical classes among the TNOs and will likely improve estimates for the trojans of Jupiter/Neptune. If other dynamical classes of TNOs or the trojans of Jupiter/Neptune have different combinations of  $(q_4, r_{max})$  than analyzed here, our approach provides a framework to test coagulation models with these new data.

Detailed tests of our coagulation calculations also assume that large-scale rearrangement of the planets in the solar system has little impact on relations between  $r_{max}$  and  $q_4$ . We do

not expect this evolution to produce significant changes in  $q_4$ . Before dynamical interactions with the gas giants become important, gravitational focusing factors are already small. Collision rates are in the orderly regime, where all objects collide at comparable rates. Thus,  $q_4$  should not evolve considerably once large-scale dynamical evolution is important.

Throughout large-scale dynamical evolution, we expect significant changes to  $q_1$ – $q_3$  as a result of collisional evolution. Because collisions remain in the orderly regime, these changes should follow the paths outlined in our discussion to Figs. 11–13. Depending on the timing of the start of the dynamical evolution,  $q_2$  and  $q_3$  for dynamically hot populations should evolve to roughly 2 or remain roughly constant at 2. If collision rates are large enough,  $q_1$  should evolve from roughly 2 to roughly 0.

Some change in  $r_{max}$  during the epoch of large-scale dynamical evolution seems likely. Because collisions occur at high velocities, it is unlikely that  $r_{max}$  increases. Low collision rates imply little collisional erosion. However, the occasional high velocity, ‘hit-and-run’ collision (Asphaug et al. 2006) could remove the outer shell of material from a large object and leave the denser core unchanged. This mechanism is one way to explain the relatively high density of Quaoar (Fraser & Brown 2010). Dynamical evolution can also eject a few of the largest TNOs from the solar system. Because the number of large objects is always small, a few ejections can reduce  $r_{max}$  and lead to variations in  $r_{max}$  among different TNO populations.

Deriving the outcome of the dynamical evolution requires codes which combine statistical calculations of small objects as in this paper with the  $n$ -body calculations of gas giant planet formation as in Bromley & Kenyon (2011a) and calculations of the migration and scattering of small objects as in Charnoz & Morbidelli (2007), Levison et al. (2008, 2010), and Bromley & Kenyon (2011b). Following the relative timing of the formation of gas giants and TNOs within the same disk will provide better limits for  $r_{max}$ ,  $q_4$ , and possible locations for the formation of TNOs within the protosolar disk. Combining collisional growth with scattering will yield better predictions for the break radius and the slope of the size distribution below the break. Our encouraging results from pure coagulation models suggest a more complete model will enable a better understanding for the origin of TNOs and other large objects throughout the solar system.

## 5. SUMMARY

To develop a framework to test coagulation models for the formation of TNOs, we have analyzed a set of calculations in grids extending from 15–75 AU and from 30–150 AU.



The calculations consider a broad range of initial conditions for (i) the disk mass ( $x_m = 0.01$ –3 times the mass of the minimum mass solar nebula), (ii) the initial size of the largest planetesimals ( $r_0 = 1, 10, \text{ and } 100 \text{ km}$ ), (iii) the initial size distribution of planetesimals ( $n_c \propto r^{-q_{init}}$ , with  $q_{init} = 0.5 \text{ and } 3$ ), and the fragmentation parameters (weak, strong, and very strong). Table 1 summarizes the number of calculations with each set of parameters.

To facilitate comparisons between the calculations and observations, we focus on several observable features of the models. The size of the largest object in a region,  $r_{max}$ , is easily derived in the models; in any survey, the brightest TNOs are usually the largest and most massive. If the albedos of TNOs are well-known, the slope of the size distribution follows from observations of the TNO luminosity function. Here, we define four quantities,  $q_1$ – $q_4$ , which measure the slope of the size distribution over a decade in radius. Tables 2–3 list median values for these slopes as a function of  $r_{max}$  for each set of initial conditions.

The evolution of  $q_1$ – $q_4$  as a function of  $r_{max}$  is equivalent to the evolution as a function of time. Thus, we treat the evolution of icy planets at all distances from the Sun on the same footing and derive more robust relations between the observables and the initial conditions. For the theoretical calculations in this paper, we infer the following conclusions (see also §3.5):

- For identical initial conditions, small variations in collision probabilities – due to different random number seeds – produce a broad range of outcomes for  $q_4$ ,  $r_{max}$ , and other observables.
- As in Kenyon & Bromley (2008, 2010), the formation time for objects with  $r = r_{max} \gtrsim 300$ –1000 km depends inversely on the initial disk mass and with the cube of the distance from the central star,  $t_f \propto x_r^{-3} a^3$  (see also Safronov 1969; Lissauer 1987; Goldreich et al. 2004).
- Coagulation models yield a robust correlation between  $r_{max}$  and  $q_4$  as a function of the initial conditions in the protosolar disk. This correlation allows unambiguous tests of the models.
- When 1000 km protoplanets grow from smaller objects, the evolution naturally leads to a roughly power-law size distribution for objects with  $r \gtrsim 100 \text{ km}$ . The typical slope for the cumulative size distribution is  $q_4 \approx 2$ –4 (see also Kenyon & Luu 1999b; Kenyon & Bromley 2004c; Schlichting & Sari 2011). This slope is independent of the distance from the Sun and the initial size distribution. Although the slope depends weakly on the fragmentation parameters, it is very sensitive to  $x_m$  and  $r_0$ . Larger  $x_m$  and larger  $r_0$  yield steeper size distributions with larger  $q_4$ .

- For planetesimal sizes smaller than the initial size of the largest planetesimal ( $r_0$ ), the size distribution retains some memory of the initial size distribution. However, this memory is limited to timescales before the onset of the collisional cascade. Once the cascade begins, the size distribution depends on the evolution of the largest objects and the fragmentation parameters for the smallest objects.
- Once protoplanets reach radii of 500–1500 km, high velocity collisions among leftover small planetesimals start a collisional cascade which grinds many of the leftovers to dust. As the cascade develops, the slopes of the size distribution for 0.1–100 km objects evolve to a standard value,  $q \approx 2.0$ –2.5. Eventually, the largest protoplanets reach sizes of 2000 km or larger. High velocity collisions among the leftovers then completely shatter 1 km and smaller objects. The slope of the size distribution for 0.1–1 km objects then evolves to much smaller values,  $q_1 \approx 0$ . Slopes for larger size ranges stay roughly constant at  $q_2 \approx q_3 \approx 2$ .

To test the ability of coagulation models to match the observations, we focus our analysis on the relation between  $q_4$  and  $r_{max}$  for the hot and cold populations of KBOs. The  $q_4$  for the cold population and the  $r_{max}$  for the hot population are representative of the entire ensemble of TNOs. Treating the two populations separately allows us to test the models as much as possible with current data.

Our tests are very encouraging. A broad range of coagulation calculations match the typical slope,  $q_4 = 5$ , for large objects when  $r_{max} = 400$ –1400 km ( $4 \times 10^{23}$  –  $1.5 \times 10^{25}$  g). Large slopes generally favor calculations starting with 10–100 km planetesimals. However, smaller  $r_{max}$  favors smaller planetesimals. The observed slope of the hot objects,  $q_4 = 3$ , completely rules out models starting with 100 km planetesimals. If TNOs must form prior to the LHB at 500–700 Myr, formation models for the hot objects require ensembles of 1 km planetesimals in a massive disk ( $x_m = 0.3$ –3). If the largest cold objects have  $r \approx 400$ –600 km ( $4 \times 10^{23}$  –  $1.5 \times 10^{24}$  g), the LHB constraint similarly requires calculations with 1 km planetesimals.

Combining the observations of the hot and cold populations with the constraints that they formed in different locations of the protosolar disk prior to 500–700 Myr leaves us with one set of starting conditions, a massive disk with 1 km planetesimals. This conclusion agrees with our previous result that the basic building blocks of debris disks are 1 km planetesimals (Kenyon & Bromley 2010). Although these analyses do not consider the possibility of 0.1 km or smaller planetesimals as in Weidenschilling (2011), the results clearly favor small planetesimals over larger planetesimals with radii of 10–100 km.

Currently, it is difficult to make robust tests of predictions for  $q_1$ – $q_3$ . Many surveys sug-

gest the TNO size distribution is a double power law with a break at  $R \approx 25\text{--}26$  (Fraser et al. 2008; Fraser & Kavelaars 2009; Fuentes et al. 2009). If TNOs have a typical albedo of 6%, the break in the size distribution is at  $r \approx 30$  km. Although the uncertainties in the observations below this break are large, the slope at small sizes is most likely shallower than at large sizes, with  $q_S \approx 2$  a reasonable estimate. The coagulation calculations described in this paper can match one of these two constraints. These calculations produce a break in the size distribution at 1–3 km (see also Kenyon & Bromley 2004c; Gil-Hutton et al. 2009; Fraser 2009). Below this break, the collisional cascade always produces a slope of roughly 2. Thus, our models in this paper match the slope below the break but not the location of the break.

Kenyon & Bromley (2004c) demonstrate that stirring from the largest nearby planet sets the ‘break radius’ (see also Gil-Hutton et al. 2009; Fraser 2009). For TNOs, continued stirring by Neptune at 30 AU yields a break at 10–30 km, close to the lower limit inferred from current observations. Given the uncertainties in the luminosity function at  $R = 25\text{--}27$  and the albedos for such TNOs, coagulation models provide a satisfactory match to the data (see also Nesvorný et al. 2011).

Improving these tests requires additional data. Among the more massive TNOs, deriving  $q_4$  and  $r_{max}$  for all of the dynamical classes will place better limits on the ability of coagulation and dynamical calculations to provide a unique model for the origin of the giant planets and TNOs. As deep surveys probe larger volumes of transneptunian space, results for the observational analogs to  $q_1\text{--}q_3$  will test the ability of coagulation models to explain size distributions for each class of TNOs. For the entire ensemble of TNOs, coagulation models probably have fewer free parameters than the set of observational constraints. Thus, TNOs should provide robust tests of coagulation models for planet formation.

We acknowledge generous allotments of computer time on the NASA ‘discover’ cluster, the SI ‘hydra’ cluster, and the ‘cosmos’ cluster at the Jet Propulsion Laboratory. We thank S. Weidenschilling for a careful and timely review. Advice and comments from W. Fraser, M. Geller, M. Holman, and A. Youdin also greatly improved our presentation. Portions of this project were supported by the *NASA Astrophysics Theory and Origins of Solar Systems* programs through grant NNX10AF35G, the *NASA TPF Foundation Science Program* through grant NNG06GH25G, the *NASA Outer Planets Program* through grant NNX11AM37G, the *Spitzer Guest Observer Program* through grant 20132, and grants from the endowment and scholarly studies programs of the Smithsonian Institution.

## A. APPENDIX

As oligarchic growth proceeds, cratering collisions gradually dominate physical interactions among 0.1–10 km planetesimals. In this regime, collisions between equal mass objects produce the most debris. For a power-law cumulative size distribution with  $q \gtrsim 3$ , small planetesimals are more likely to collide with one another than with large oligarchs (Kenyon & Bromley 2004a; Goldreich et al. 2004). Thus, cratering leads to a gradual erosion of small planetesimals (e.g., Tanaka & Ida 1996; Kobayashi & Tanaka 2010).

During this erosive phase, collisions between equal mass objects produce a single object with mass comparable to the target and copious debris. For these objects, the slope of the size distribution then depends on the rate collisions convert planetesimals into debris and the rate of debris production over a range of sizes. To estimate the rate planetesimals are lost, we consider the collision rate,  $n\sigma v f_g$ . During oligarchic growth, small planetesimals have similar orbital eccentricities and  $f_g \approx 1$ . For collisions between equal mass objects, the rate small planetesimals are destroyed is  $dN/dt \propto N^2 r^2$ , where  $N$  is the number of planetesimals in a size range and  $r$  is a typical radius. Setting  $N \propto r^{-q}$ ,

$$d \log N/dt \approx r^{2-q} . \quad (\text{A1})$$

For an ensemble of planetesimals, small objects are destroyed relatively more (less) often when  $q \gtrsim 2$  ( $q \lesssim 2$ ). More destructive collisions among small objects reduces the slope; fewer destructive collisions raises the slope. Without any debris, this process leads to an equilibrium size distribution with  $q \approx 2$ . In our simulations, debris has a power-law cumulative size distribution with  $q_{debris} = 2.5$ . Thus, cratering produces a power-law size distribution with  $q_{cr} \approx 2.0$ – $2.5$ , as observed in our calculations.

As the largest objects continue to grow, collisions among small objects become more and more catastrophic. For the fragmentation parameters we adopt,  $Q_D^*$  monotonically increases with  $r$  for  $\gtrsim 0.1$  km. In this range, small objects fragment catastrophically before large objects. Thus, catastrophic fragmentation reduces the equilibrium slope from the cratering slope of 2.0–2.5.

To provide a rough estimate of the equilibrium slope for catastrophic collisions, we consider a collision rate where the fraction of completely destructive collisions is a decreasing function of  $r$ , e.g.,  $f_d \propto r^{-p}$ . The loss rate of planetesimals is then,

$$d \log N/dt \approx f_d r^{2-q} \approx r^{2-p-q} . \quad (\text{A2})$$

From the expression for  $Q_D^*$  (eq. [6]),  $p \approx 1.5$ . In the absence of debris production, catastrophic collisions lead to a power-law size distribution with  $q_{cd} \approx 0.5$ , close to the  $q \approx 0$ – $1$  derived in our simulations.

## REFERENCES

- Adachi, I., Hayashi, C., & Nakazawa, K. 1976, *Progress of Theoretical Physics*, 56, 1756
- Alibert, Y., Mousis, O., Mordasini, C., & Benz, W. 2005, *ApJ*, 626, L57
- Andrews, S. M., & Williams, J. P. 2005, *ApJ*, 631, 1134
- Arakawa, M., Leliwa-Kopystynski, J., & Maeno, N. 2002, *Icarus*, 158, 516
- Asphaug, E., Agnor, C. B., & Williams, Q. 2006, *Nature*, 439, 155
- Batygin, K., Brown, M. E., & Betts, H. 2011a, *ArXiv e-prints*
- Batygin, K., Brown, M. E., & Fraser, W. C. 2011b, *ApJ*, 738, 13
- Belyaev, M. A., & Rafikov, R. R. 2011, *Icarus*, 214, 179
- Benavidez, P. G., & Campo Bagatin, A. 2009, *Planet. Space Sci.*, 57, 201
- Benz, W., & Asphaug, E. 1999, *Icarus*, 142, 5
- Bernstein, G. M., Trilling, D. E., Allen, R. L., Brown, M. E., Holman, M., & Malhotra, R. 2004, *AJ*, 128, 1364
- Birnstiel, T., Dullemond, C. P., & Brauer, F. 2010, *A&A*, 513, A79+
- Bromley, B. C., & Kenyon, S. J. 2006, *AJ*, 131, 2737
- . 2011a, *ApJ*, 731, 101
- . 2011b, *ApJ*, 735, 29
- Brown, M. E., & Schaller, E. L. 2007, *Science*, 316, 1585
- Brucker, M. J., Grundy, W. M., Stansberry, J. A., Spencer, J. R., Sheppard, S. S., Chiang, E. I., & Buie, M. W. 2009, *Icarus*, 201, 284
- Buie, M. W., Grundy, W. M., Young, E. F., Young, L. A., & Stern, S. A. 2006, *AJ*, 132, 290
- Burchell, M. J., Leliwa-Kopystynski, J., & Arakawa, M. 2005, *Icarus*, 179, 274
- Chambers, J. E. 2010, *Icarus*, 208, 505
- Chapman, C. R., Cohen, B. A., & Grinspoon, D. H. 2007, *Icarus*, 189, 233
- Charnoz, S., & Morbidelli, A. 2007, *Icarus*, 188, 468

- Chiang, E., & Youdin, A. N. 2010, *Annual Review of Earth and Planetary Sciences*, 38, 493
- Currie, T., Lada, C. J., Plavchan, P., Robitaille, T. P., Irwin, J., & Kenyon, S. J. 2009, *ApJ*, 698, 1
- Cuzzi, J. N., Hogan, R. C., & Bottke, W. F. 2010, *Icarus*, 208, 518
- Davis, D. R., Chapman, C. R., Weidenschilling, S. J., & Greenberg, R. 1985, *Icarus*, 63, 30
- Davis, D. R., Farinella, P., & Weidenschilling, S. J. 1999, in *Lunar and Planetary Institute Science Conference Abstracts*, Vol. 30, Lunar and Planetary Institute Science Conference Abstracts, 1883
- Dohnanyi, J. S. 1969, *J. Geophys. Res.*, 74, 2531
- Fraser, W. C. 2009, *ApJ*, 706, 119
- Fraser, W. C., & Brown, M. E. 2010, *ApJ*, 714, 1547
- Fraser, W. C., Brown, M. E., & Schwamb, M. E. 2010, *Icarus*, 210, 944
- Fraser, W. C., & Kavelaars, J. J. 2009, *AJ*, 137, 72
- Fraser, W. C., et al. 2008, *Icarus*, 195, 827
- Fuentes, C. I., George, M. R., & Holman, M. J. 2009, *ApJ*, 696, 91
- Fuentes, C. I., & Holman, M. J. 2008, *AJ*, 136, 83
- Fuentes, C. I., Trilling, D. E., & Holman, M. J. 2011, *ArXiv e-prints*
- Giblin, I., Davis, D. R., & Ryan, E. V. 2004, *Icarus*, 171, 487
- Gil-Hutton, R., Licandro, J., Pinilla-Alonso, N., & Brunetto, R. 2009, *A&A*, 500, 909
- Gladman, B., Marsden, B. G., & Vanlaerhoven, C. 2008, *Nomenclature in the Outer Solar System*, ed. Barucci, M. A., Boehnhardt, H., Cruikshank, D. P., Morbidelli, A., & Dotson, R., 43–57
- Goldreich, P., Lithwick, Y., & Sari, R. 2004, *ARA&A*, 42, 549
- Gomes, R., Levison, H. F., Tsiganis, K., & Morbidelli, A. 2005, *Nature*, 435, 466
- Gomes, R. S. 2003, *Icarus*, 161, 404
- Greenberg, R., Bottke, W. F., Carusi, A., & Valsecchi, G. B. 1991, *Icarus*, 94, 98

- Greenzweig, Y., & Lissauer, J. J. 1992, *Icarus*, 100, 440
- Grundy, W. M., Noll, K. S., Buie, M. W., Benecchi, S. D., Stephens, D. C., & Levison, H. F. 2009, *Icarus*, 200, 627
- Grundy, W. M., et al. 2011, *Icarus*, 213, 678
- Gulbis, A. A. S., Elliot, J. L., & Kane, J. F. 2006, *Icarus*, 183, 168
- Hahn, J. M., & Malhotra, R. 1999, *AJ*, 117, 3041
- Haisch, Jr., K. E., Lada, E. A., & Lada, C. J. 2001, *ApJ*, 553, L153
- Hartmann, W. K., Ryder, G., Dones, L., & Grinspoon, D. 2000, *The Time-Dependent Intense Bombardment of the Primordial Earth/Moon System*, ed. Canup, R. M., Righter, K., & et al., 493–512
- Hayashi, C. 1981, *Progress of Theoretical Physics Supplement*, 70, 35
- Ida, S., & Lin, D. N. C. 2008, *ApJ*, 673, 487
- Inaba, S., Wetherill, G. W., & Ikoma, M. 2003, *Icarus*, 166, 46
- Jedicke, R., Larsen, J., & Spahr, T. 2002, *Asteroids III*, 71
- Jewitt, D. C., Trujillo, C. A., & Luu, J. X. 2000, *AJ*, 120, 1140
- Johansen, A., Oishi, J. S., Mac Low, M.-M., Klahr, H., Henning, T., & Youdin, A. 2007, *Nature*, 448, 1022
- Kennedy, G. M., & Kenyon, S. J. 2008, *ApJ*, 673, 502
- . 2009, *ApJ*, 695, 1210
- Kenyon, S. J. 2002, *PASP*, 114, 265
- Kenyon, S. J., & Bromley, B. C. 2001, *AJ*, 121, 538
- . 2002, *AJ*, 123, 1757
- . 2004a, *AJ*, 127, 513
- . 2004b, *ApJ*, 602, L133
- . 2004c, *AJ*, 128, 1916

- . 2005, *AJ*, 130, 269
- . 2008, *ApJS*, 179, 451
- . 2009, *ApJ*, 690, L140
- . 2010, *ApJS*, 188, 242
- Kenyon, S. J., Bromley, B. C., O’Brien, D. P., & Davis, D. R. 2008, in *The Solar System Beyond Neptune*, ed. Barucci, M. A., Boehnhardt, H., Cruikshank, D. P., Morbidelli, A., & Dotson, R. (University of Arizona Press, Tucson, AZ), 293–313
- Kenyon, S. J., & Hartmann, L. 1987, *ApJ*, 323, 714
- Kenyon, S. J., & Luu, J. X. 1998, *AJ*, 115, 2136
- . 1999a, *AJ*, 118, 1101
- . 1999b, *ApJ*, 526, 465
- Kobayashi, H., & Tanaka, H. 2010, *Icarus*, 206, 735
- Krivov, A. V., Sremčević, M., & Spahn, F. 2005, *Icarus*, 174, 105
- Lee, M. H. 2000, *Icarus*, 143, 74
- Leinhardt, Z. M., & Stewart, S. T. 2009, *Icarus*, 199, 542
- Leinhardt, Z. M., Stewart, S. T., & Schultz, P. H. 2008, in *The Solar System Beyond Neptune*, ed. Barucci, M. A., Boehnhardt, H., Cruikshank, D. P., Morbidelli, A., & Dotson, R., 195–211
- Levison, H. F., Dones, L., Chapman, C. R., Stern, S. A., Duncan, M. J., & Zahnle, K. 2001, *Icarus*, 151, 286
- Levison, H. F., & Morbidelli, A. 2003, *Nature*, 426, 419
- Levison, H. F., Morbidelli, A., Vanlaerhoven, C., Gomes, R., & Tsiganis, K. 2008, *Icarus*, 196, 258
- Levison, H. F., & Stern, S. A. 2001, *AJ*, 121, 1730
- Levison, H. F., Thommes, E., & Duncan, M. J. 2010, *AJ*, 139, 1297
- Lissauer, J. J. 1987, *Icarus*, 69, 249



- Lissauer, J. J., Hubickyj, O., D'Angelo, G., & Bodenheimer, P. 2009, *Icarus*, 199, 338
- Malhotra, R. 1993, *Nature*, 365, 819
- . 1995, *AJ*, 110, 420
- Mamajek, E. E. 2009, in *American Institute of Physics Conference Series*, Vol. 1158, American Institute of Physics Conference Series, ed. T. Usuda, M. Tamura, & M. Ishii, 3–10
- Morbidelli, A., Emel'yanenko, V. V., & Levison, H. F. 2004, *MNRAS*, 355, 935
- Morbidelli, A., Levison, H. F., Bottke, W. F., Dones, L., & Nesvorný, D. 2009, *Icarus*, 202, 310
- Morbidelli, A., Levison, H. F., & Gomes, R. 2008, in *The Solar System Beyond Neptune* (The University of Arizona Press), 275–292
- Morbidelli, A., Levison, H. F., Tsiganis, K., & Gomes, R. 2005, *Nature*, 435, 462
- Murray-Clay, R. A., & Schlichting, H. E. 2011, *ApJ*, 730, 132
- Nesvorný, D., Vokrouhlický, D., Bottke, W. F., Noll, K., & Levison, H. F. 2011, *AJ*, 141, 159
- Noll, K. S., Grundy, W. M., Stephens, D. C., Levison, H. F., & Kern, S. D. 2008, *Icarus*, 194, 758
- O'Brien, D. P., & Greenberg, R. 2003, *Icarus*, 164, 334
- O'Brien, D. P., Morbidelli, A., & Bottke, W. F. 2005, in *Bulletin of the American Astronomical Society*, 676
- Ohtsuki, K. 1992, *Icarus*, 98, 20
- Ohtsuki, K., Stewart, G. R., & Ida, S. 2002, *Icarus*, 155, 436
- Pan, L., Padoan, P., Scalo, J., Kritsuk, A. G., & Norman, M. L. 2011, *ApJ*, 740, 6
- Pan, M., & Sari, R. 2005, *Icarus*, 173, 342
- Peixinho, N., Boehnhardt, H., Belskaya, I., Doressoundiram, A., Barucci, M. A., & Delsanti, A. 2004, *Icarus*, 170, 153
- Peixinho, N., Lacerda, P., & Jewitt, D. 2008, *AJ*, 136, 1837

- Petit, J.-M., Holman, M. J., Gladman, B. J., Kavelaars, J. J., Scholl, H., & Loredano, T. J. 2006, *MNRAS*, 365, 429
- Petit, J.-M., Kavelaars, J. J., Gladman, B., & Loredano, T. 2008, in *The Solar System Beyond Neptune* (The University of Arizona Press), 71–87
- Petit, J.-M., et al. 2011, ArXiv e-prints
- Pollack, J. B., Hubickyj, O., Bodenheimer, P., Lissauer, J. J., Podolak, M., & Greenzweig, Y. 1996, *Icarus*, 124, 62
- Rafikov, R. R. 2004, *AJ*, 128, 1348
- Ryan, E. V., Davis, D. R., & GIBLIN, I. 1999, *Icarus*, 142, 56
- Safronov, V. S. 1969, *Evolutsiia doplanetnogo oblaka*. (Evolution of the Protoplanetary Cloud and Formation of the Earth and Planets, Nauka, Moscow [Translation 1972, NASA TT F-677] (1969.))
- Schlichting, H. E., & Sari, R. 2011, *ApJ*, 728, 68
- Schwamb, M. E., Brown, M. E., Rabinowitz, D. L., & Ragozzine, D. 2010, *ApJ*, 720, 1691
- Sheppard, S., et al. 2011, *AJ*, 142, 98
- Sheppard, S. S., & Trujillo, C. A. 2010, *ApJ*, 723, L233
- Spaute, D., Weidenschilling, S. J., Davis, D. R., & Marzari, F. 1991, *Icarus*, 92, 147
- Stansberry, J., Grundy, W., Brown, M., Cruikshank, D., Spencer, J., Trilling, D., & Margot, J.-L. 2008, *Physical Properties of Kuiper Belt and Centaur Objects: Constraints from the Spitzer Space Telescope*, ed. Barucci, M. A., Boehnhardt, H., Cruikshank, D. P., Morbidelli, A., & Dotson, R., 161–179
- Stern, S. A., & Colwell, J. E. 1997a, *AJ*, 114, 841
- . 1997b, *ApJ*, 490, 879
- Stöfler, D., & Ryder, G. 2001, *Space Sci. Rev.*, 96, 9
- Strom, R. G., Malhotra, R., Ito, T., Yoshida, F., & Kring, D. A. 2005, *Science*, 309, 1847
- Tanaka, H., & Ida, S. 1996, *Icarus*, 120, 371
- Tanaka, H., & Nakazawa, K. 1994, *Icarus*, 107, 404

- Tegler, S. C., & Romanishin, W. 2000, *Nature*, 407, 979
- Tera, F., Papanastassiou, D. A., & Wasserburg, G. J. 1974, *Earth and Planetary Science Letters*, 22, 1
- Trujillo, C. A., & Brown, M. E. 2002, *ApJ*, 566, L125
- Tsiganis, K., Gomes, R., Morbidelli, A., & Levison, H. F. 2005, *Nature*, 435, 459
- Weidenschilling, S. J. 1977a, *MNRAS*, 180, 57
- . 1977b, *Ap&SS*, 51, 153
- . 1989, *Icarus*, 80, 179
- . 1997, *Icarus*, 127, 290
- . 2006, *Icarus*, 181, 572
- . 2011, *Icarus*, 214, 671
- Weidenschilling, S. J., Spaute, D., Davis, D. R., Marzari, F., & Ohtsuki, K. 1997, *Icarus*, 128, 429
- Wetherill, G. W. 1990, *Icarus*, 88, 336
- Wetherill, G. W., & Stewart, G. R. 1993, *Icarus*, 106, 190
- Williams, D. R., & Wetherill, G. W. 1994, *Icarus*, 107, 117
- Williams, J. P., & Cieza, L. A. 2011, *ArXiv e-prints*
- Wolff, S., Dawson, R. I., & Murray-Clay, R. A. 2011, *ArXiv e-prints*

Table 1. Grid of Calculations<sup>a</sup> with  $\Sigma \propto a^{-3/2}$

$x_m$	Initial size of largest object ( $r_0$ )										
	1 km	10 km	100 km	1 km	10 km	100 km	1 km	10 km	100 km	1 km	1 km
0.01	7	7	7	7	14	7	7	8	10	14	15
0.03	7	7	7	7	7	7	7	8	9	16	15
0.10	7	7	7	7	12	7	7	7	8	14	15
0.33	7	7	7	8	14	9	7	7	15	19	17
1.00	7	7	7	8	16	7	14	7	13	15	16
3.00	7	7	7	7	7	7	13	7	13	18	15
Notes	b, e, g	b, e, g	b, e, g	c, e, g	c, e, g	c, e, g	c, f, g	c, f, g	c, f, g	c, f, h	d, f, i

<sup>a</sup>Number of independent calculations for each combination of  $x_m$  and  $r_0$

<sup>b</sup> $a = 15\text{--}75$  AU,  $t_{max} = 1$  Gyr, new calculations for this paper

<sup>c</sup> $a = 30\text{--}150$  AU,  $t_{max} = 10$  Gyr, calculations from Kenyon & Bromley (2008, 2010)

<sup>d</sup> $a = 30\text{--}150$  AU,  $t_{max} = 10$  Gyr, new calculations for this paper

<sup>e</sup> $n_c \propto r^{-0.5}$

<sup>f</sup> $n_c \propto r^{-3}$

<sup>g</sup> $f_w$  fragmentation parameters (Leinhardt & Stewart 2009)

<sup>h</sup> $f_s$  fragmentation parameters (Benz & Asphaug 1999)

<sup>i</sup> $f_{vs}$  fragmentation parameters (Davis et al. 1985)

Table 2. Median values for  $q_4$  when  $r_{max} = 1000$  km

Parameter	Initial Disk Mass ( $x_m$ )						Notes
	0.01	0.03	0.10	0.33	1.00	3.00	
$q_{4,3}$	1.78	2.08	3.62	4.13	5.06	5.30	$a = 15\text{--}75$ AU, $r_0 = 1$ km, $n_c \propto r^{-0.5}$ , $f_W$
$q_{4,3}$	...	3.86	4.39	4.69	5.61	5.60	$a = 15\text{--}75$ AU, $r_0 = 10$ km, $n_c \propto r^{-0.5}$ , $f_W$
$q_{4,3}$	...	...	...	5.25	6.27	6.53	$a = 15\text{--}75$ AU, $r_0 = 100$ km, $n_c \propto r^{-0.5}$ , $f_W$
$q_{4,3}$	1.83	2.79	3.64	5.48	6.31	6.22	$a = 30\text{--}150$ AU, $r_0 = 1$ km, $n_c \propto r^{-0.5}$ , $f_W$
$q_{4,3}$	...	3.72	4.50	4.94	5.65	5.53	$a = 30\text{--}150$ AU, $r_0 = 10$ km, $n_c \propto r^{-0.5}$ , $f_W$
$q_{4,3}$	...	...	5.03	5.42	6.61	6.93	$a = 30\text{--}150$ AU, $r_0 = 100$ km, $n_c \propto r^{-0.5}$ , $f_W$
$q_{4,3}$	...	2.74	2.94	2.93	3.53	4.08	$a = 30\text{--}150$ AU, $r_0 = 1$ km, $n_c \propto r^{-3}$ , $f_W$
$q_{4,3}$	...	2.72	3.73	4.68	5.18	5.70	$a = 30\text{--}150$ AU, $r_0 = 10$ km, $n_c \propto r^{-3}$ , $f_W$
$q_{4,3}$	...	3.52	4.03	4.74	5.12	5.63	$a = 30\text{--}150$ AU, $r_0 = 100$ km, $n_c \propto r^{-3}$ , $f_W$
$q_{4,3}$	1.85	2.18	2.58	3.17	3.55	4.25	$a = 30\text{--}150$ AU, $r_0 = 1$ km, $n_c \propto r^{-3}$ , $f_S$
$q_{4,3}$	...	2.52	2.98	3.08	3.81	4.24	$a = 30\text{--}150$ AU, $r_0 = 1$ km, $n_c \propto r^{-3}$ , $f_{vs}$

Table 3. Median values for  $q_1$  when  $r_{max} = 1000$  km

Parameter	Initial Disk Mass ( $x_m$ )						Notes
	0.01	0.03	0.10	0.33	1.00	3.00	
$q_{1,3}$	1.97	2.00	1.28	1.13	1.06	1.29	$a = 15\text{--}75$ AU, $r_0 = 1$ km, $n_c \propto r^{-0.5}$ , $f_W$
$q_{1,3}$	...	2.23	2.23	2.24	2.26	2.26	$a = 15\text{--}75$ AU, $r_0 = 10$ km, $n_c \propto r^{-0.5}$ , $f_W$
$q_{1,3}$	...	...	...	1.99	2.06	1.91	$a = 15\text{--}75$ AU, $r_0 = 100$ km, $n_c \propto r^{-0.5}$ , $f_W$
$q_{1,3}$	2.04	1.56	1.34	1.19	1.25	1.40	$a = 30\text{--}150$ AU, $r_0 = 1$ km, $n_c \propto r^{-0.5}$ , $f_W$
$q_{1,3}$	...	2.25	2.25	2.25	2.25	2.26	$a = 30\text{--}150$ AU, $r_0 = 10$ km, $n_c \propto r^{-0.5}$ , $f_W$
$q_{1,3}$	...	...	2.06	1.98	2.16	1.78	$a = 30\text{--}150$ AU, $r_0 = 100$ km, $n_c \propto r^{-0.5}$ , $f_W$
$q_{1,3}$	...	2.42	2.17	2.15	2.20	2.34	$a = 30\text{--}150$ AU, $r_0 = 1$ km, $n_c \propto r^{-3}$ , $f_W$
$q_{1,3}$	...	2.18	2.28	2.39	2.18	2.20	$a = 30\text{--}150$ AU, $r_0 = 10$ km, $n_c \propto r^{-3}$ , $f_W$
$q_{1,3}$	...	2.14	2.14	2.12	2.11	2.10	$a = 30\text{--}150$ AU, $r_0 = 100$ km, $n_c \propto r^{-3}$ , $f_W$
$q_{1,3}$	2.03	2.26	2.22	2.41	2.43	2.41	$a = 30\text{--}150$ AU, $r_0 = 1$ km, $n_c \propto r^{-3}$ , $f_S$
$q_{1,3}$	...	2.39	2.51	2.29	2.31	2.37	$a = 30\text{--}150$ AU, $r_0 = 1$ km, $n_c \propto r^{-3}$ , $f_{vs}$

Table 4. Median values for  $q_2$  when  $r_{max} = 1000$  km

Parameter	Initial Disk Mass ( $x_m$ )						Notes
	0.01	0.03	0.10	0.33	1.00	3.00	
$q_{2,3}$	3.25	3.18	3.63	3.64	3.61	3.51	$a = 15\text{--}75$ AU, $r_0 = 1$ km, $n_c \propto r^{-0.5}$ , $f_W$
$q_{2,3}$	...	0.94	0.89	0.89	0.91	1.02	$a = 15\text{--}75$ AU, $r_0 = 10$ km, $n_c \propto r^{-0.5}$ , $f_W$
$q_{2,3}$	...	...	...	2.27	2.24	2.24	$a = 15\text{--}75$ AU, $r_0 = 100$ km, $n_c \propto r^{-0.5}$ , $f_W$
$q_{2,3}$	3.30	3.59	3.61	3.66	3.50	3.35	$a = 30\text{--}150$ AU, $r_0 = 1$ km, $n_c \propto r^{-0.5}$ , $f_W$
$q_{2,3}$	...	0.95	0.90	0.93	1.13	1.05	$a = 30\text{--}150$ AU, $r_0 = 10$ km, $n_c \propto r^{-0.5}$ , $f_W$
$q_{2,3}$	...	...	2.25	2.26	2.22	2.25	$a = 30\text{--}150$ AU, $r_0 = 100$ km, $n_c \propto r^{-0.5}$ , $f_W$
$q_{2,3}$	...	4.03	3.70	3.72	4.00	3.83	$a = 30\text{--}150$ AU, $r_0 = 1$ km, $n_c \propto r^{-3}$ , $f_W$
$q_{2,3}$	...	2.96	3.12	3.14	3.14	3.15	$a = 30\text{--}150$ AU, $r_0 = 10$ km, $n_c \propto r^{-3}$ , $f_W$
$q_{2,3}$	...	2.56	2.61	2.69	2.70	2.73	$a = 30\text{--}150$ AU, $r_0 = 100$ km, $n_c \propto r^{-3}$ , $f_W$
$q_{2,3}$	4.44	4.11	4.00	3.94	4.00	3.92	$a = 30\text{--}150$ AU, $r_0 = 1$ km, $n_c \propto r^{-3}$ , $f_S$
$q_{2,3}$	...	4.15	4.00	3.97	4.05	4.08	$a = 30\text{--}150$ AU, $r_0 = 1$ km, $n_c \propto r^{-3}$ , $f_{vs}$

Table 5. Median values for  $q_3$  when  $r_{max} = 1000$  km

Parameter	Initial Disk Mass ( $x_m$ )						Notes
	0.01	0.03	0.10	0.33	1.00	3.00	
$q_{3,3}$	4.17	4.14	3.85	3.82	3.71	3.70	$a = 15\text{--}75$ AU, $r_0 = 1$ km, $n_c \propto r^{-0.5}$ , $f_W$
$q_{3,3}$	...	4.11	4.05	4.06	4.05	3.98	$a = 15\text{--}75$ AU, $r_0 = 10$ km, $n_c \propto r^{-0.5}$ , $f_W$
$q_{3,3}$	...	...	...	0.97	0.93	0.95	$a = 15\text{--}75$ AU, $r_0 = 100$ km, $n_c \propto r^{-0.5}$ , $f_W$
$q_{3,3}$	3.87	3.72	3.67	3.64	3.70	3.69	$a = 30\text{--}150$ AU, $r_0 = 1$ km, $n_c \propto r^{-0.5}$ , $f_W$
$q_{3,3}$	...	4.03	4.06	4.02	3.96	3.94	$a = 30\text{--}150$ AU, $r_0 = 10$ km, $n_c \propto r^{-0.5}$ , $f_W$
$q_{3,3}$	...	...	0.93	0.97	0.90	0.92	$a = 30\text{--}150$ AU, $r_0 = 100$ km, $n_c \propto r^{-0.5}$ , $f_W$
$q_{3,3}$	...	3.18	3.43	3.19	2.93	3.40	$a = 30\text{--}150$ AU, $r_0 = 1$ km, $n_c \propto r^{-3}$ , $f_W$
$q_{3,3}$	...	3.87	3.86	3.82	3.67	3.71	$a = 30\text{--}150$ AU, $r_0 = 10$ km, $n_c \propto r^{-3}$ , $f_W$
$q_{3,3}$	...	3.16	3.15	3.16	3.16	3.17	$a = 30\text{--}150$ AU, $r_0 = 100$ km, $n_c \propto r^{-3}$ , $f_W$
$q_{3,3}$	2.91	3.20	3.34	3.36	3.25	3.35	$a = 30\text{--}150$ AU, $r_0 = 1$ km, $n_c \propto r^{-3}$ , $f_S$
$q_{3,3}$	...	3.44	3.84	3.69	3.59	3.45	$a = 30\text{--}150$ AU, $r_0 = 1$ km, $n_c \propto r^{-3}$ , $f_{vs}$

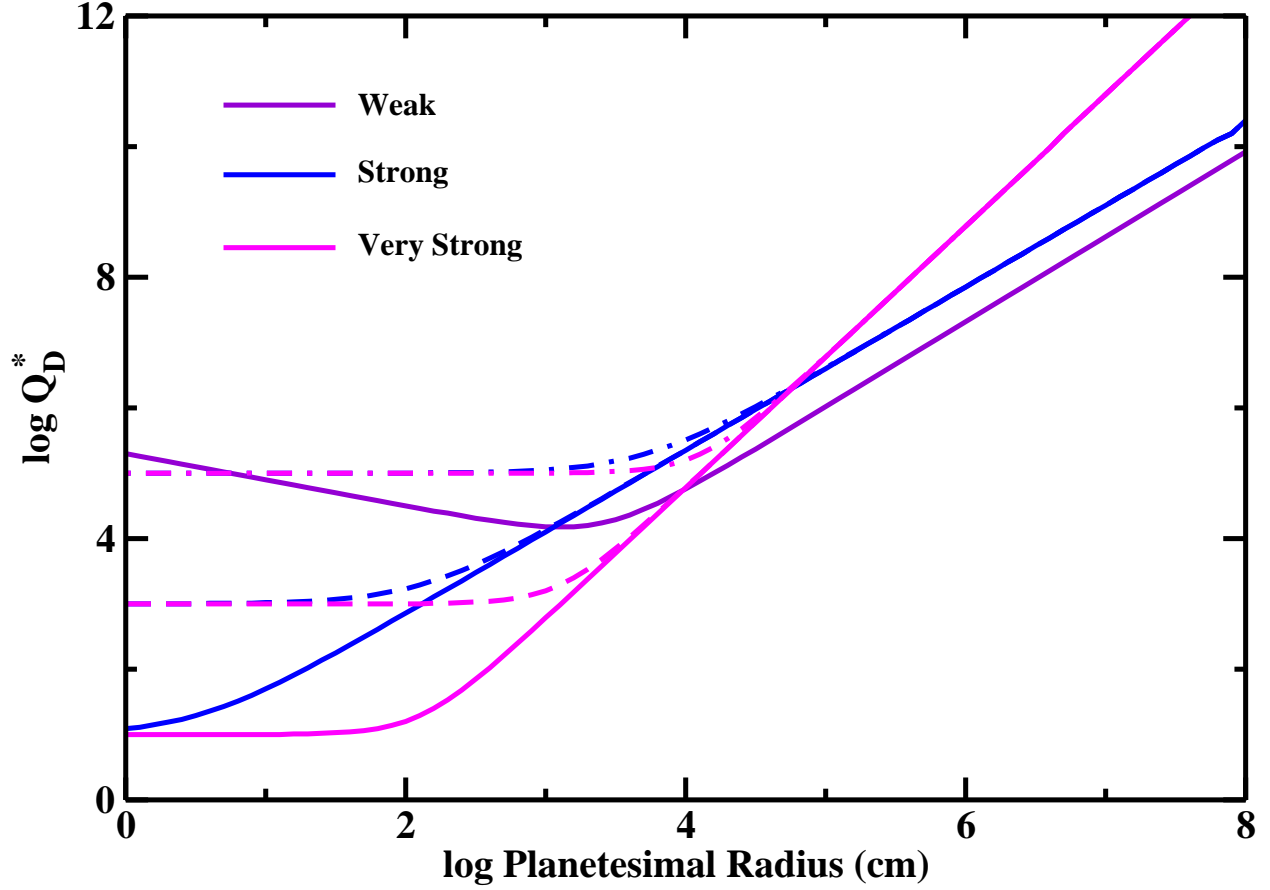


Fig. 1.— Variation of  $Q_D^*$  with radius for the three sets of fragmentation parameters adopted in the text. For the strong and very strong planetesimals, the solid ( $Q_b = 10$ ), dashed ( $Q_b = 10^3$ ) and dot-dashed curves ( $Q_b = 10^5$ ) indicate a range of parameters for the strength regime.

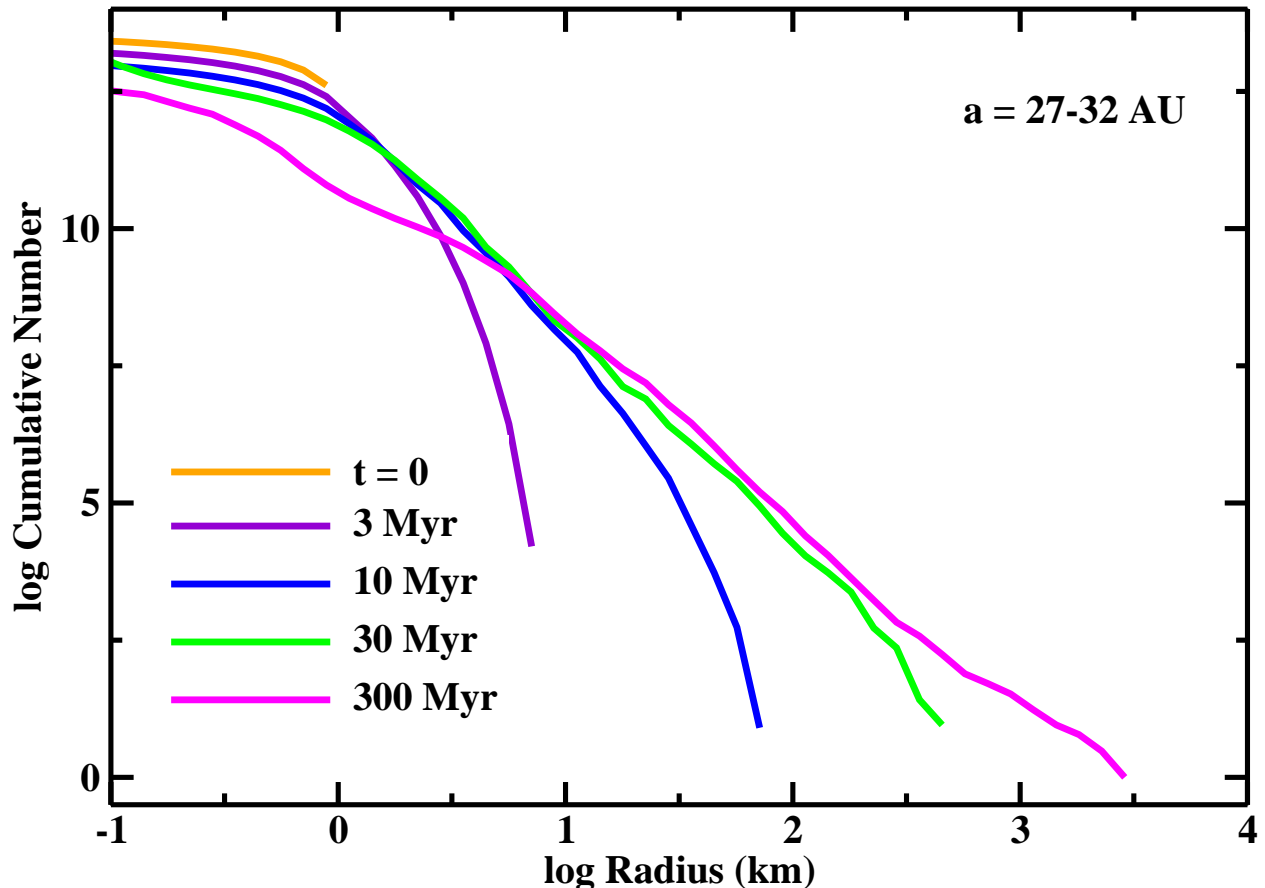


Fig. 2.— Time evolution of the cumulative number distribution for 8 annuli ( $a = 27\text{--}32$  AU) in a disk with initial surface density distribution  $\Sigma = 0.18 x_m (a/30 \text{ AU})^{-3/2} \text{ g cm}^{-2}$ ,  $x_m = 1$ , and the  $f_w$  fragmentation parameters. The ensemble of planetesimals has an initial cumulative size distribution  $n_c \propto r^{-0.5}$  with a maximum radius of 1 km; thus, most of the initial mass is in the largest objects. During runaway growth at 1–10 Myr, the largest protoplanets grow from  $\sim 10$  km to  $\sim 1000$  km. At the same time, the slope of the size distribution becomes shallower and shallower. At late times ( $t \gtrsim 100$  Myr), the size distribution is a fairly smooth power law from  $\sim 3\text{--}10$  km to  $\sim 3000$  km.



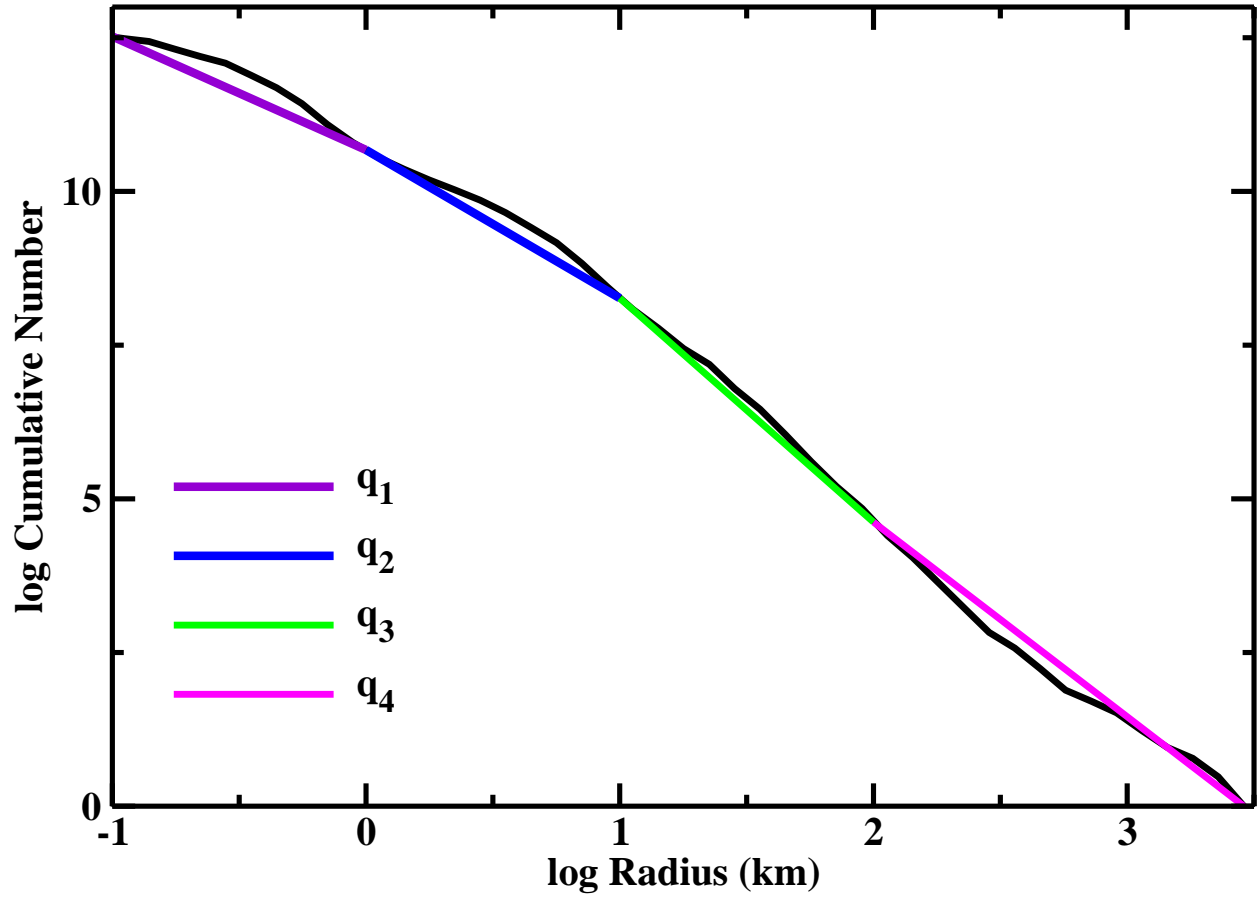


Fig. 3.— Definitions of the four slope parameters defined in the text. The black curve repeats the 300 Myr size distribution from Fig. 2. The slopes  $q_1$ - $q_4$  are the slopes of the four line segments in the figure.

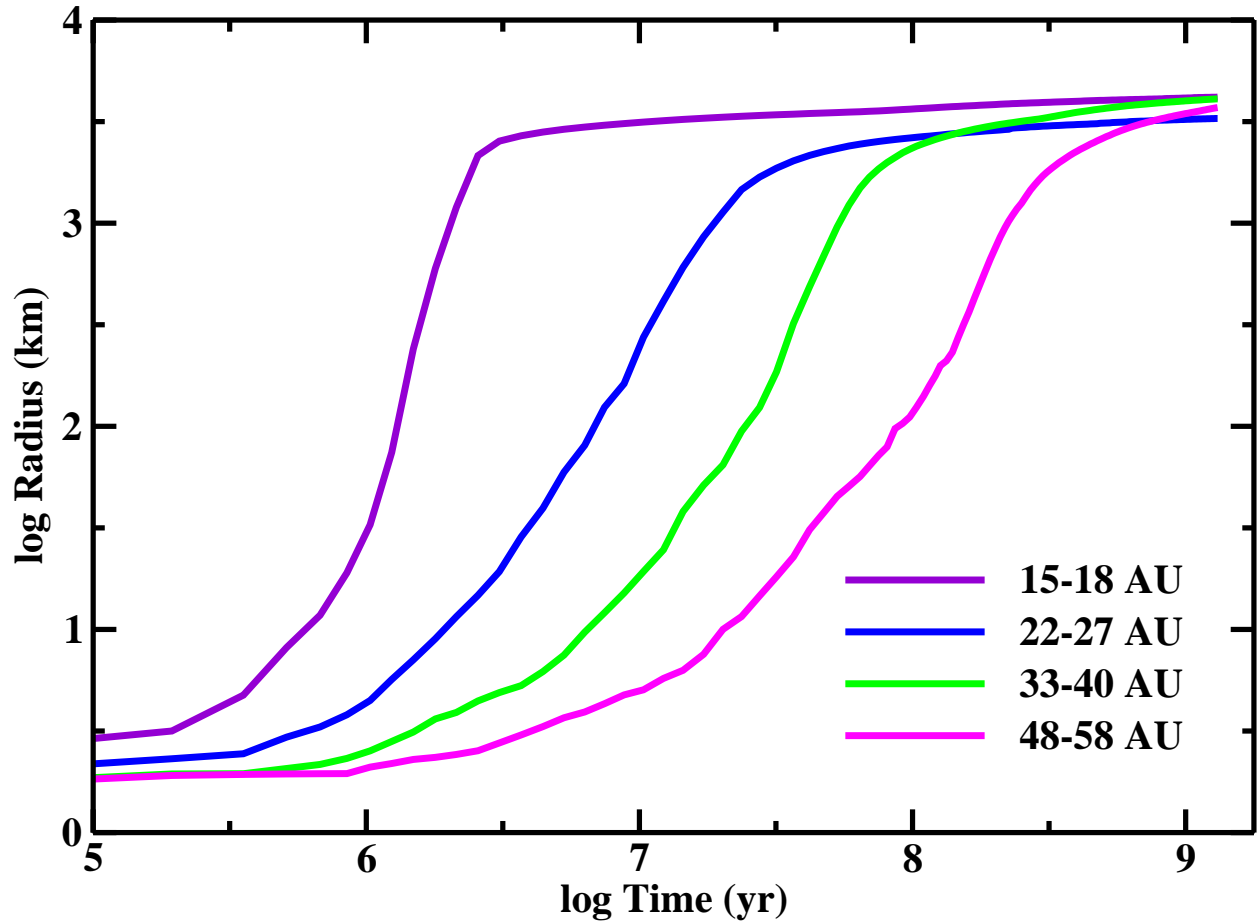


Fig. 4.— Time evolution of the size of the largest object in 4 sets of eight annuli for the calculation described in Fig. 2. After a short period of slow growth, objects rapidly grow from  $\sim 10$  km to  $\sim 1000$  km (runaway growth) and then grow more slowly to  $\sim 3000$ – $5000$  km (oligarchic growth). Objects close to the central star grow faster. In roughly 1 Gyr, however, all objects reach a characteristic maximum radius of 3000–5000 km.

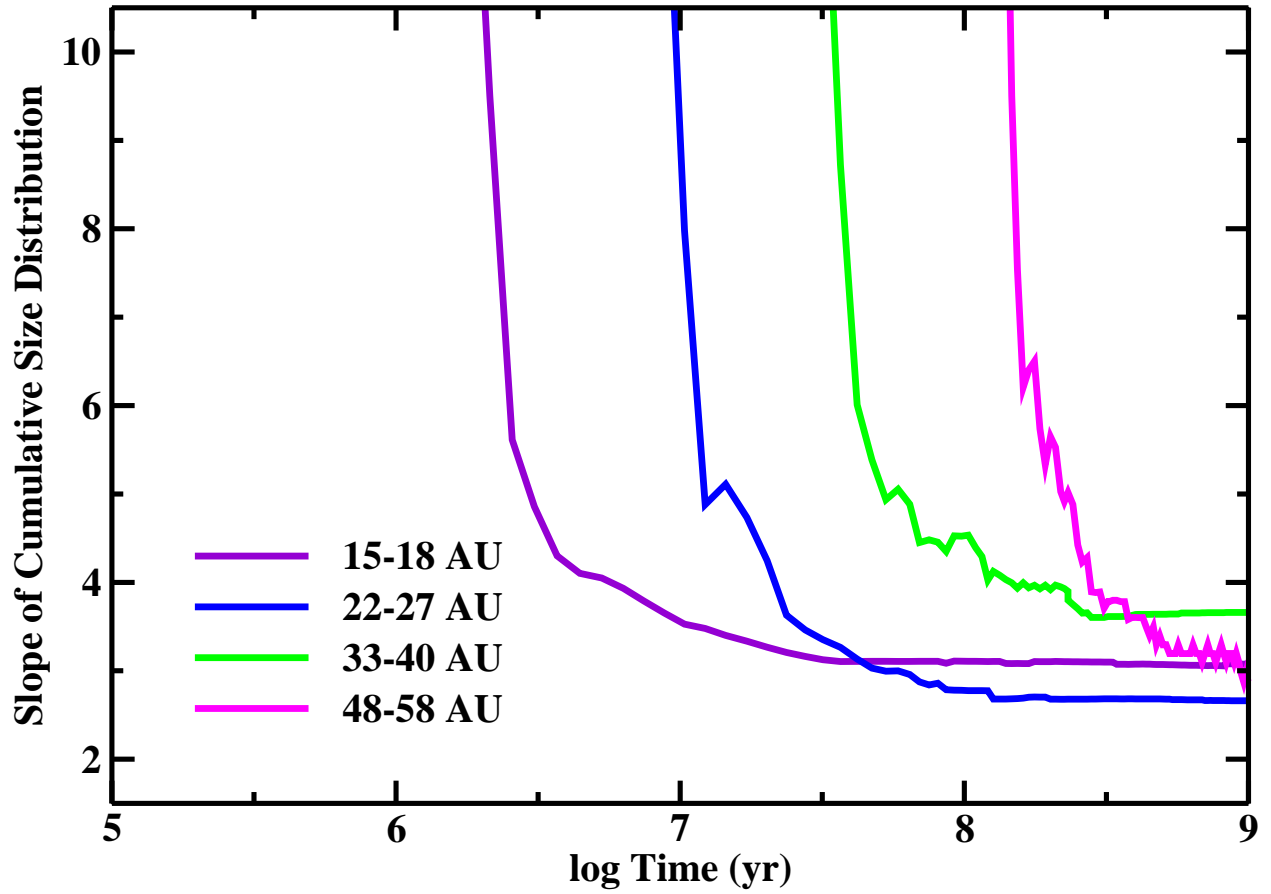


Fig. 5.— As in Fig. 4 for the slope of the cumulative size distribution. During runaway growth, the slope decreases rapidly from  $q \gtrsim 10$  to  $q \approx 4$ . As oligarchic growth proceeds, the slope asymptotically approaches  $q \approx 3$ . Noise in the plots results from counting statistics in the mass bins.

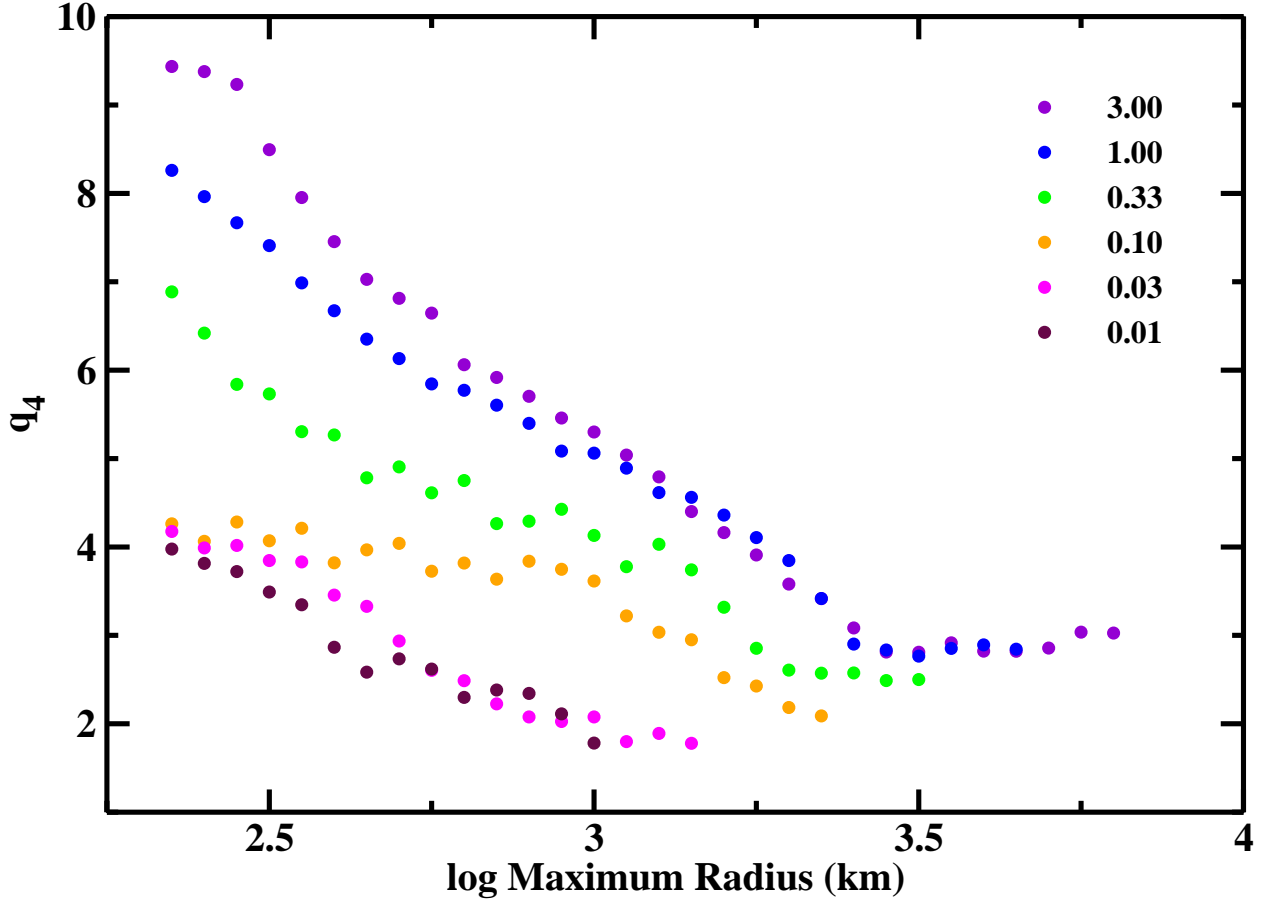


Fig. 6.— Variation of the median  $q_4$  with  $r_{max}$  for all annuli at all times in an ensemble of disks at 15–75 AU starting with most of the mass in the largest planetesimals and the  $f_w$  fragmentation parameters. The legend indicates  $x_m$ , the scaling factor for the initial surface density (eq. [4]). The typical inter-quartile range is roughly  $\delta q_{igr} \approx 2$  at  $\log r_{max} \approx 2.25-2.75$  and  $\delta q_{igr} \approx 0.5-1.0$  at  $\log r_{max} \gtrsim 3$ . For all  $x_m$ , the absolute lower bound in the slope is  $q_4 \approx 2$ . The upper bound has  $q_4$  roughly inversely proportional to  $r_{max}$  and slowly decreasing with  $x_m$ . In calculations with smaller  $x_m$ , slower growth allows the slope to reach the lower bound when the largest objects are relatively small.

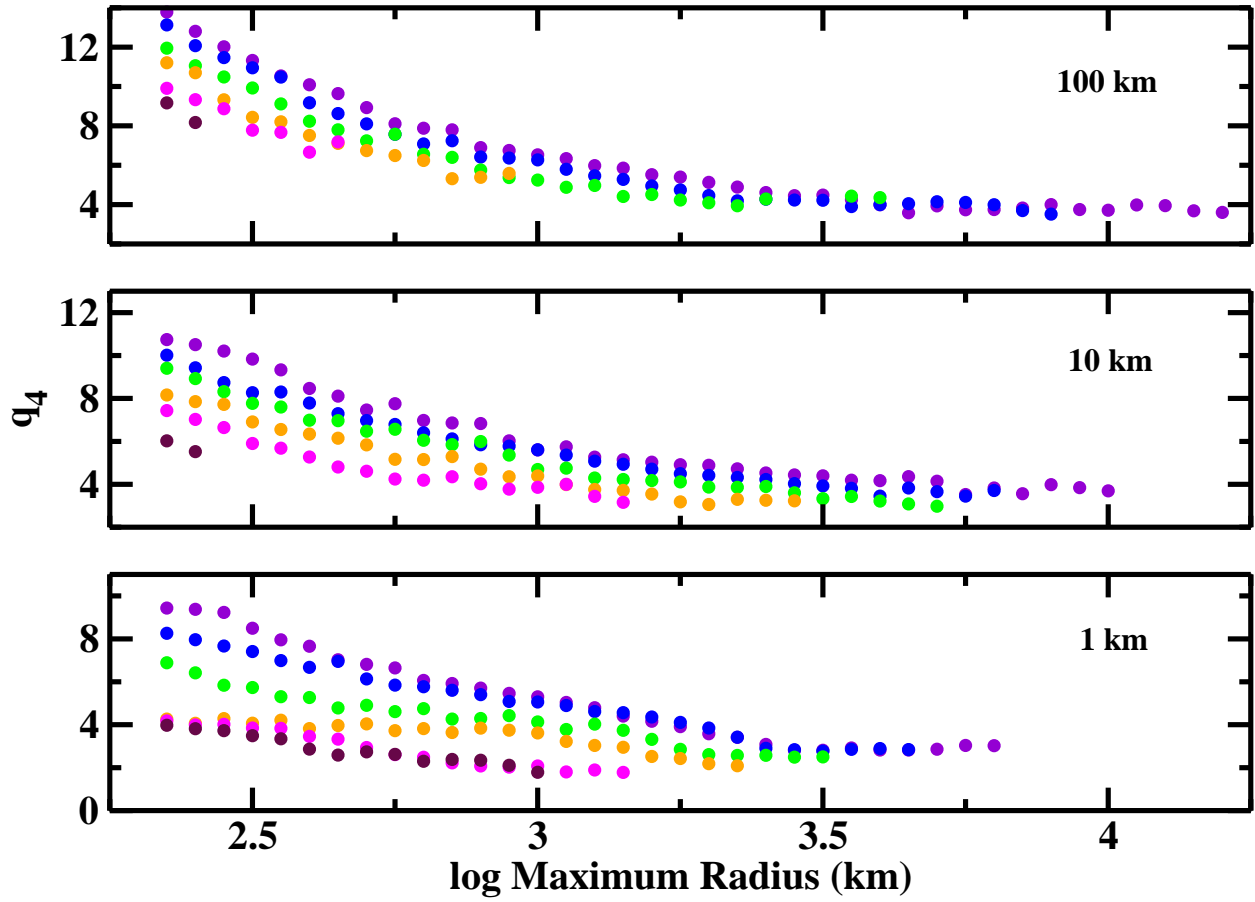


Fig. 7.— As in Fig. 6 for calculations with larger planetesimals. The lower panel repeats Fig. 6. The legend indicates the initial radius of the largest planetesimals. Compared to calculations with 1 km planetesimals, calculations with 10–100 km planetesimals yield larger planets and larger  $q_4$  at fixed  $\log r_{max}$ .

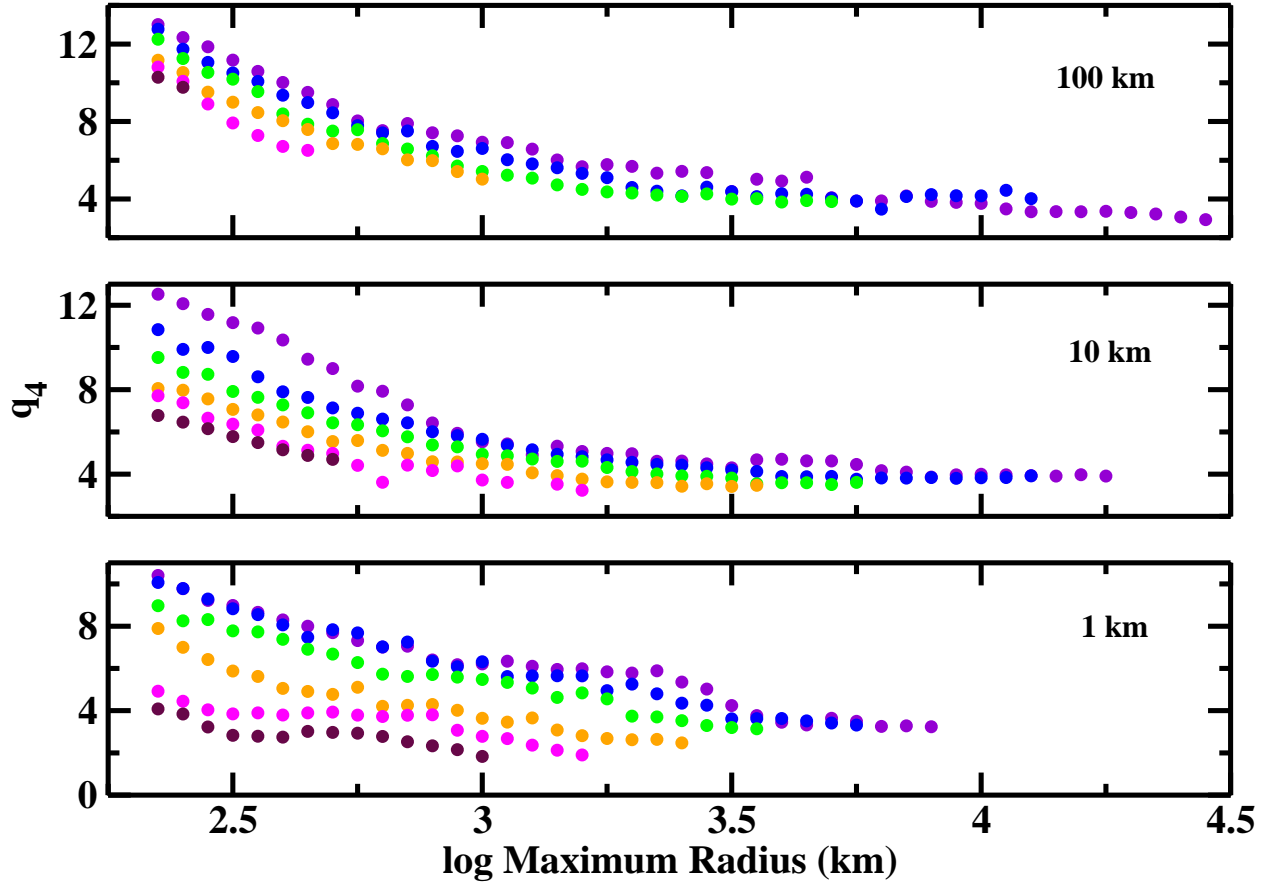


Fig. 8.— As in Fig. 7 for disks at 30–150 AU over a 10 Gyr evolution time. Results at 30–150 AU yield the same relationship for  $q_4$  as a function of  $r_{max}$  and  $x_m$ . Longer evolution times in calculations at 30–150 AU produce larger  $r_{max}$  than the calculations at 15–75 AU.

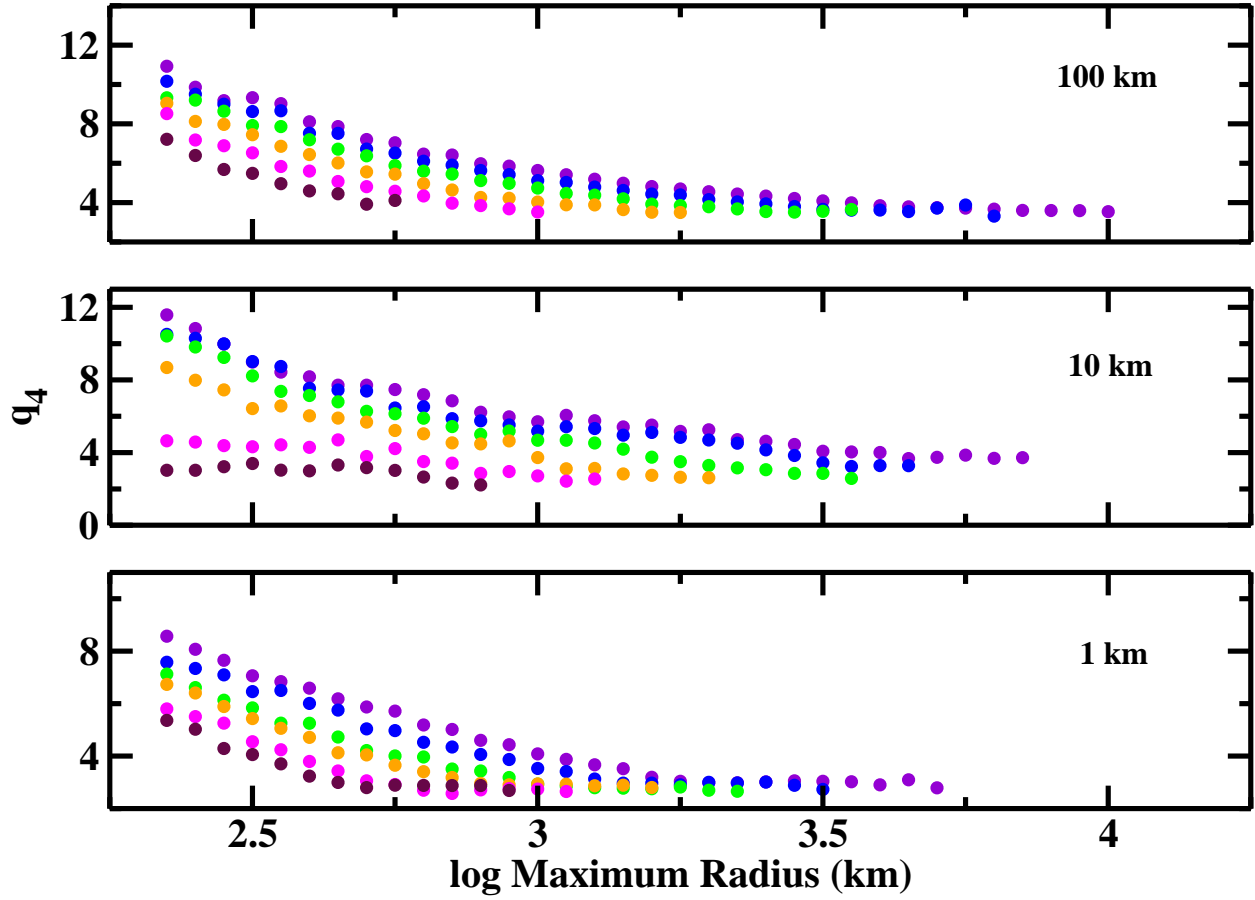


Fig. 9.— As in Fig. 8 for disks at 30–150 AU starting with a mix of planetesimal sizes and the  $f_w$  fragmentation parameters. Calculations with a broader initial size distribution yield less massive planets and a shallower relation between  $q_4$  and  $r_{max}$ . For a fixed  $r_{max}$ , calculations with larger  $r_0$  have steeper size distributions.

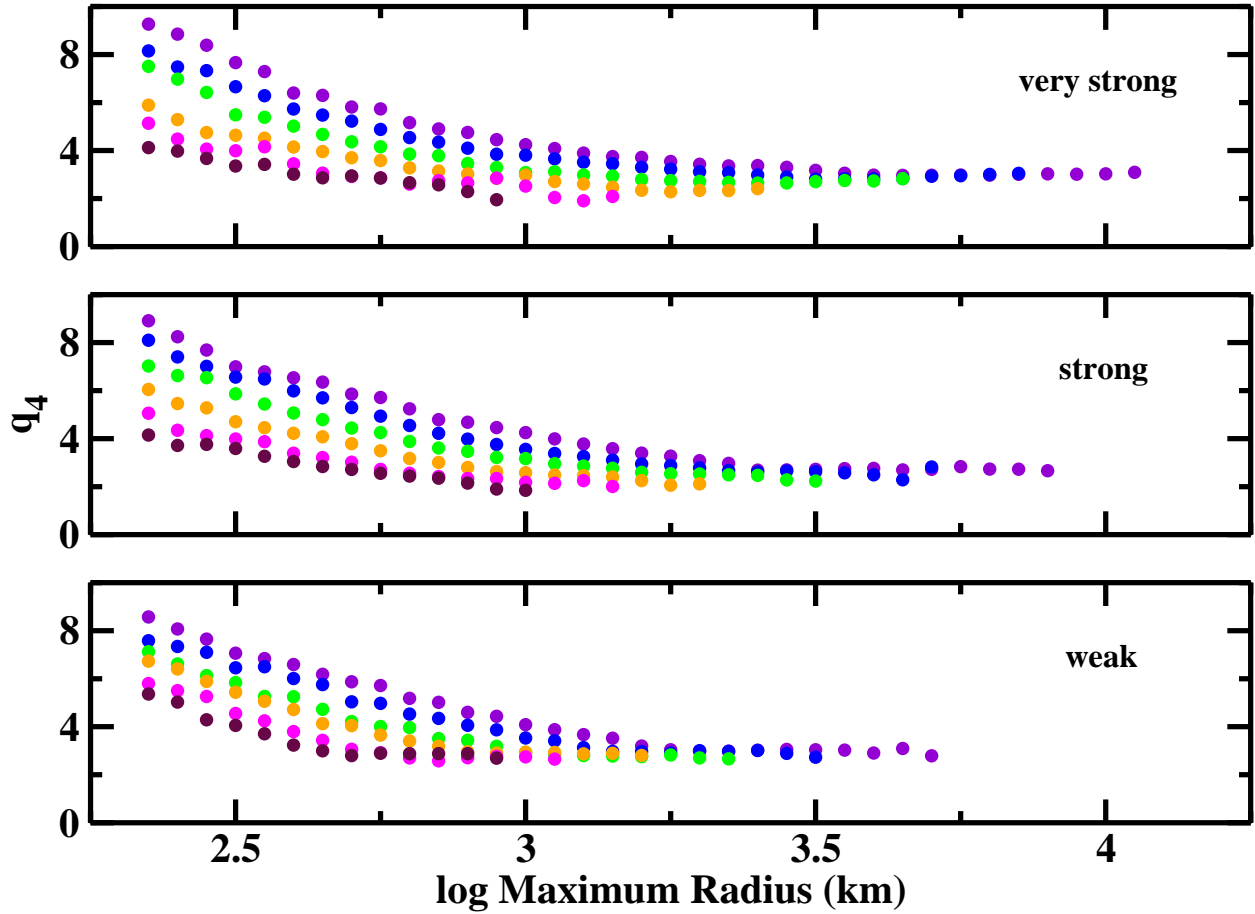


Fig. 10.— As in Fig. 9 for calculations at 30–150 AU with the  $f_w$  (lower panel),  $f_s$  (middle panel), and  $f_{vs}$  (upper panel) fragmentation parameters. All calculations begin with a broad initial size distribution of planetesimals and  $r_0 = 1$  km. Calculations with weaker planetesimals yield less massive planets.



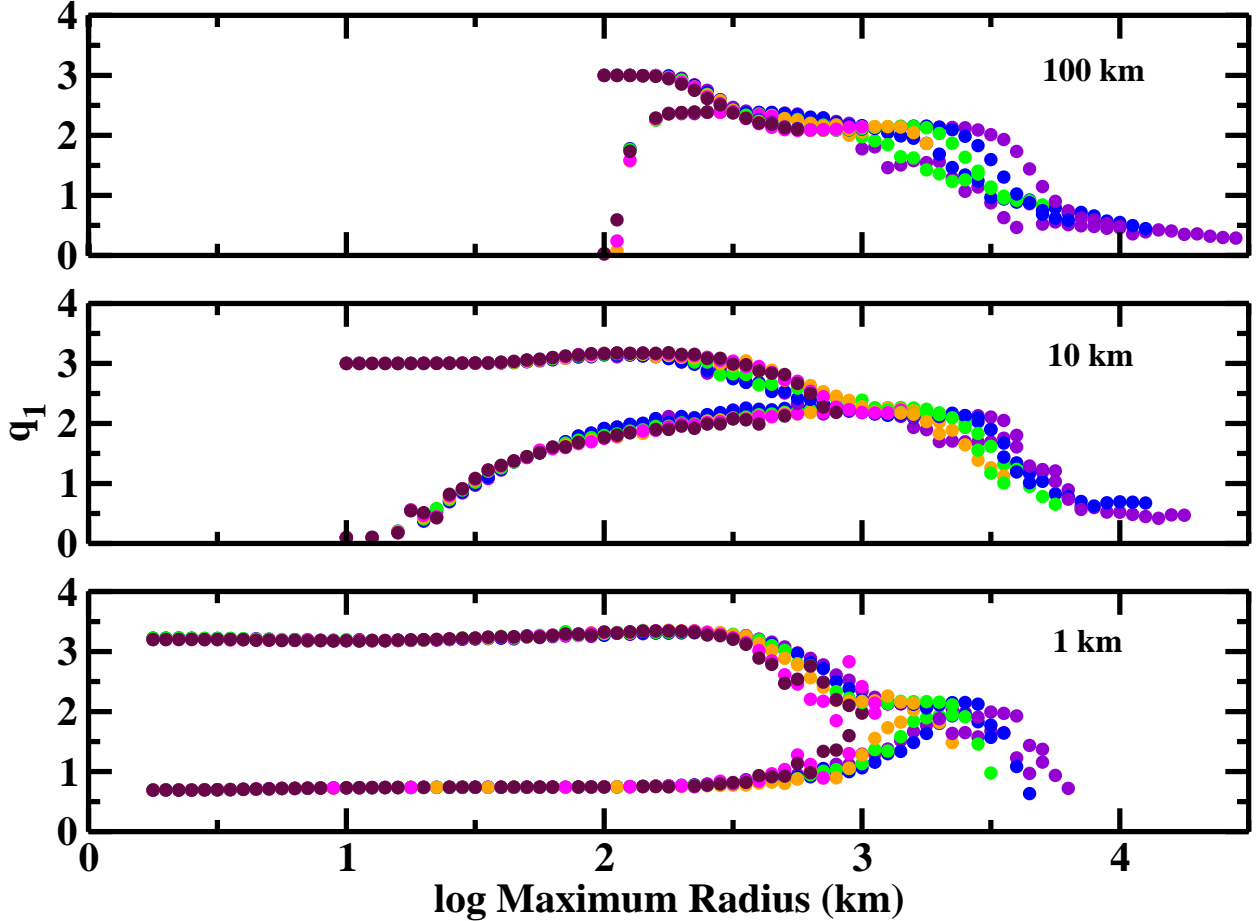


Fig. 11.— Variation of the median  $q_1$  with  $r_{max}$  for calculations of disks at 30–150 AU, the  $f_w$  fragmentation parameters, and  $r_0 = 1$  km (lower panel), 10 km (middle panel), and 100 km (upper panel). Results for calculations with  $n_c \propto r^{-3}$  (upper branch of points in each panel) and  $n_c \propto r^{-0.5}$  (lower branch of points in each panel) are included in all panels. Colors indicate results for different values of  $x_m$  as in Fig. 6. The evolution of the slope is remarkably independent of  $r_0$ . Until the onset of the collisional cascade at  $\log r_{max} \approx 2.5$ –3, calculations ‘remember’ the initial slope of the size distribution at 0.1–1 km. Once the collisional cascade begins, the slope rapidly evolves to  $q_1 \approx 2$ . As  $r_{max}$  reaches  $\sim 3000$  km, the slope declines to  $q_1 \approx 0.0$ –0.5.

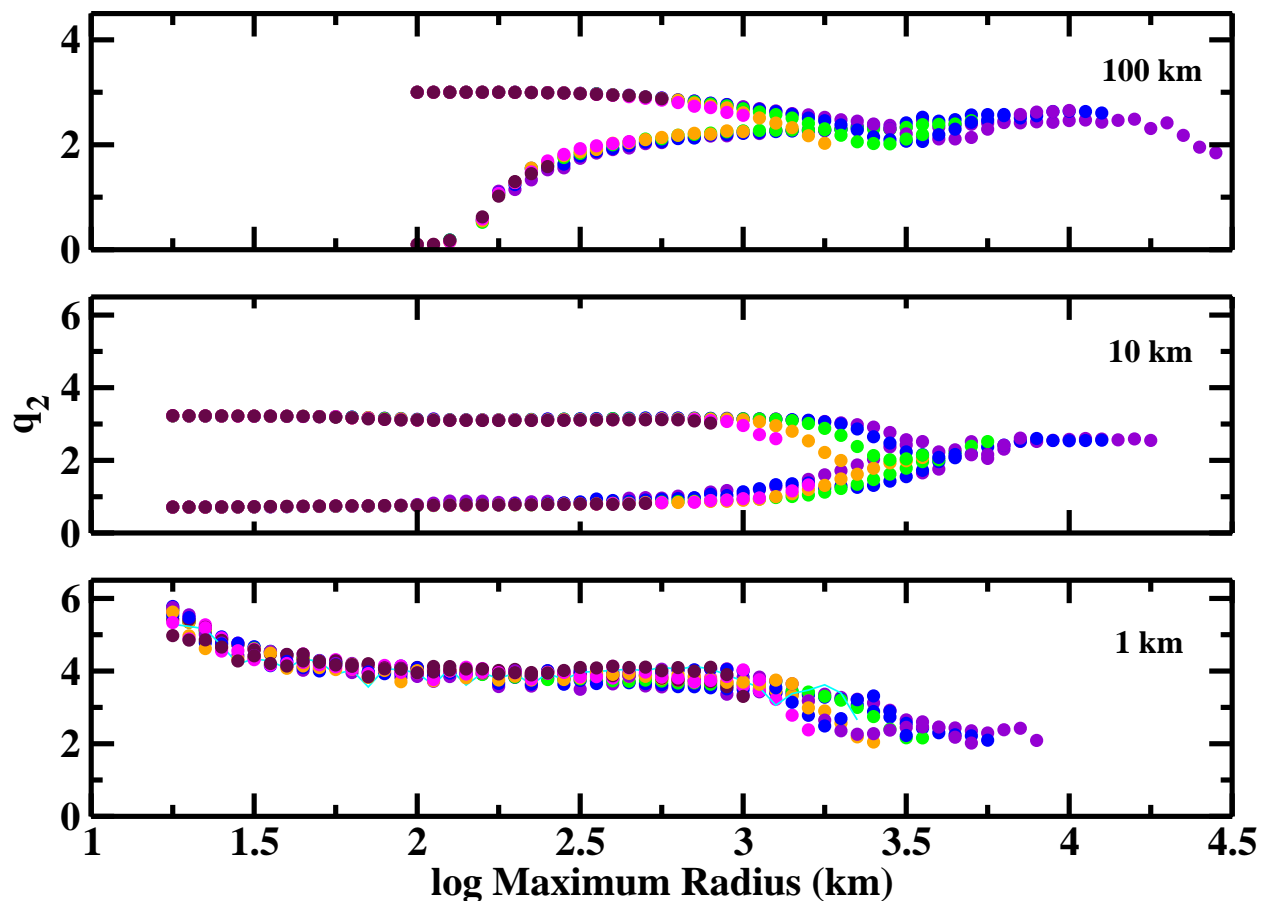


Fig. 12.— As in Fig. 11 for  $q_2$ , the slope of the size distribution at 1–10 km. For calculations with small  $r_0$ , the evolution of  $q_2$  is independent of the slope of the initial size distribution at smaller sizes; as  $r_{max}$  grows from  $\sim 30$  km to  $\sim 1000$  km,  $q_2$  monotonically declines from  $q_2 \approx 5$ –6 to  $q_2 \approx 4$ . When  $r_0$  is larger,  $q_2$  remains close to its initial value until the onset of the collisional cascade at  $\log r_{max} \approx 3$ . When the cascade begins,  $q_2$  evolves to  $\sim 2$  and remains close to this value independent of  $r_{max}$ .

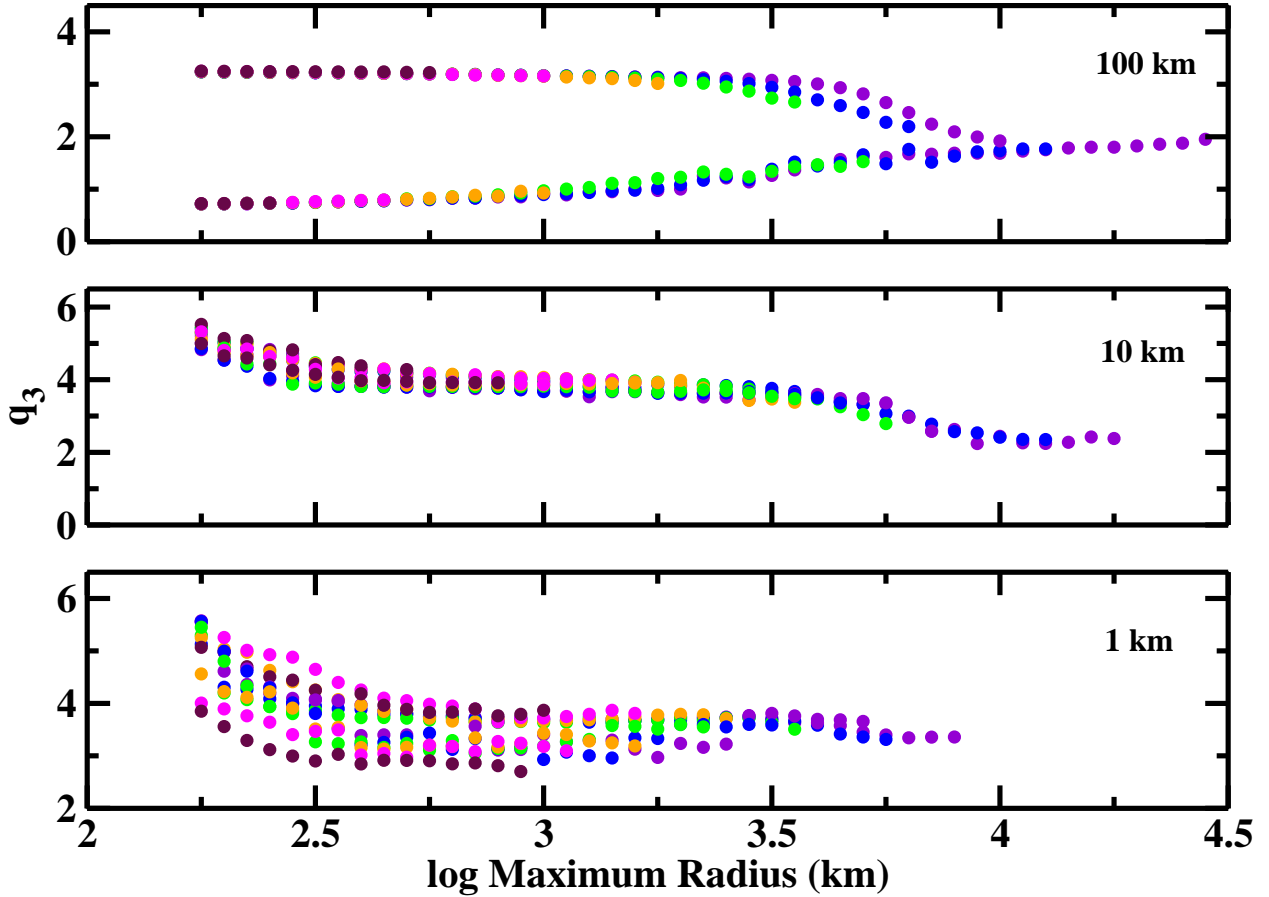


Fig. 13.— As in Fig. 11 for  $q_3$ , the slope of the size distribution at 10–100 km. For calculations with  $r_0 \lesssim 10$  km, the evolution of  $q_3$  is independent of the slope of the initial size distribution at smaller sizes; as  $r_{max}$  grows from  $\sim 300$  km to  $\sim 1000$  km,  $q_3$  monotonically declines from  $q_3 \approx 5-6$  to  $q_3 \approx 3-4$ . At any  $\log r_{max} \lesssim 3$ , the variation in  $q_3$  with  $x_m$  is larger for calculations with smaller  $r_0$ . Once the collisional cascade begins, the slope slowly evolves to  $q_3 \approx 2-3$ , with  $q_3 \approx 2$  favored at late times.

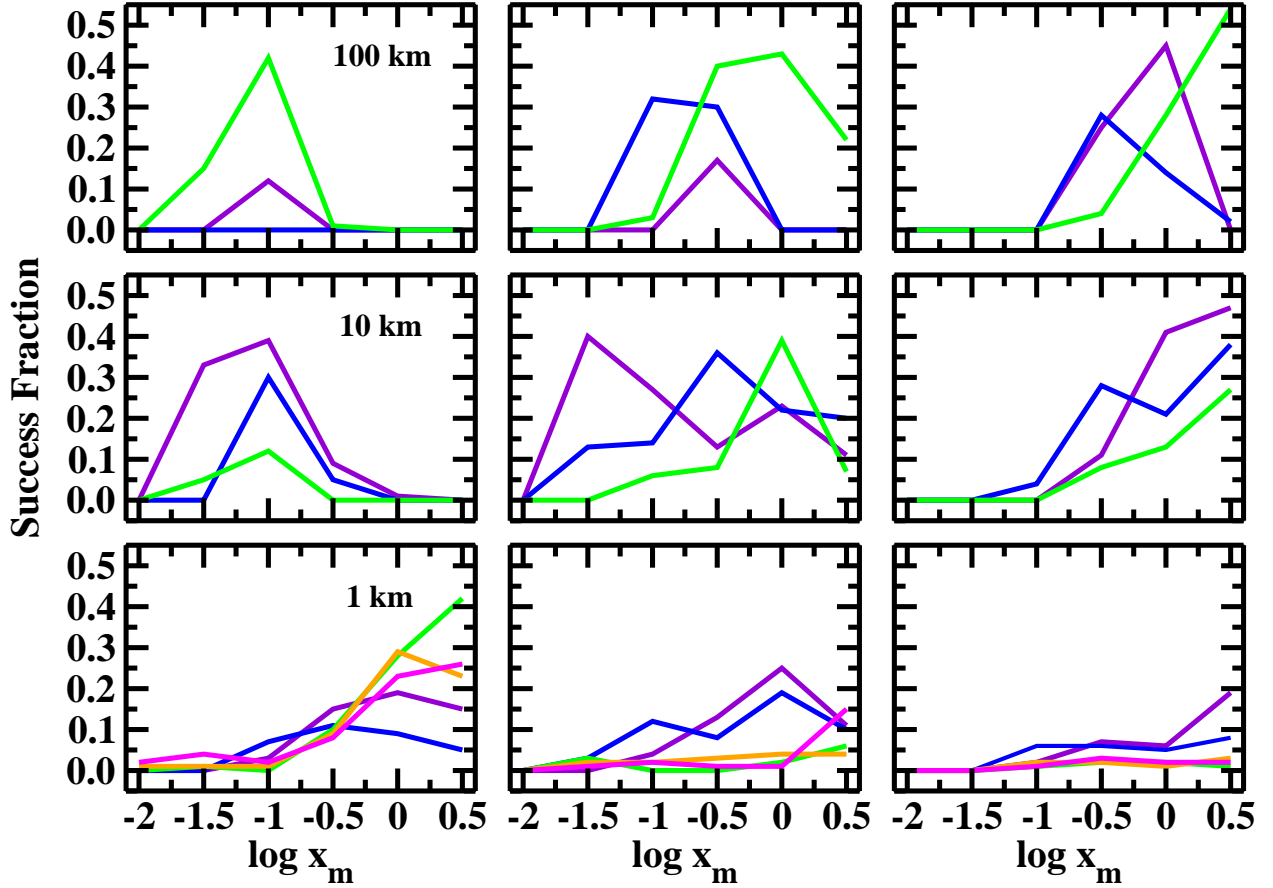


Fig. 14.— Fraction of calculations that achieve a target slope  $q_4 = 5 \pm 0.25$  and maximum size  $\log r_{max} = 2.80 \pm 0.05$  (left panels),  $\log r_{max} = 3.00 \pm 0.05$  (middle panels), or  $\log r_{max} = 3.15 \pm 0.05$  (right panels) as a function of the initial disk mass ( $x_m$ ). In each panel, the legend indicates  $r_0$ . Colored lines show results for different starting conditions; violet:  $a = 15\text{--}75$  AU;  $n_c \propto r^{-0.5}$ ,  $f_w$  fragmentation parameters; blue:  $a = 30\text{--}150$  AU;  $n_c \propto r^{-0.5}$ ,  $f_w$  fragmentation parameters; green:  $a = 30\text{--}150$  AU;  $n_c \propto r^{-3}$ ,  $f_w$  fragmentation parameters; orange:  $a = 30\text{--}150$  AU;  $n_c \propto r^{-3}$ ,  $f_s$  fragmentation parameters; magenta:  $a = 30\text{--}150$  AU;  $n_c \propto r^{-3}$ ,  $f_{vs}$  fragmentation parameters. For  $r_0 = 1$  km (lower panels), any range of  $a$ , most initial disk masses, and all fragmentation parameters, 10% to 30% of the calculations achieve the target slope and maximum radius; the success rate decreases slowly with  $r_{max}$ . For  $r_0 = 10$  km (middle panels) and  $r_0 = 100$  km (upper panels), 20% to 50% of calculations with larger disk masses ( $x_m \gtrsim 0.3$ ) – but none of the calculations with smaller disk masses ( $x_m \lesssim 0.3$ ) reach the target; the success rate increases slowly with  $r_{max}$ .

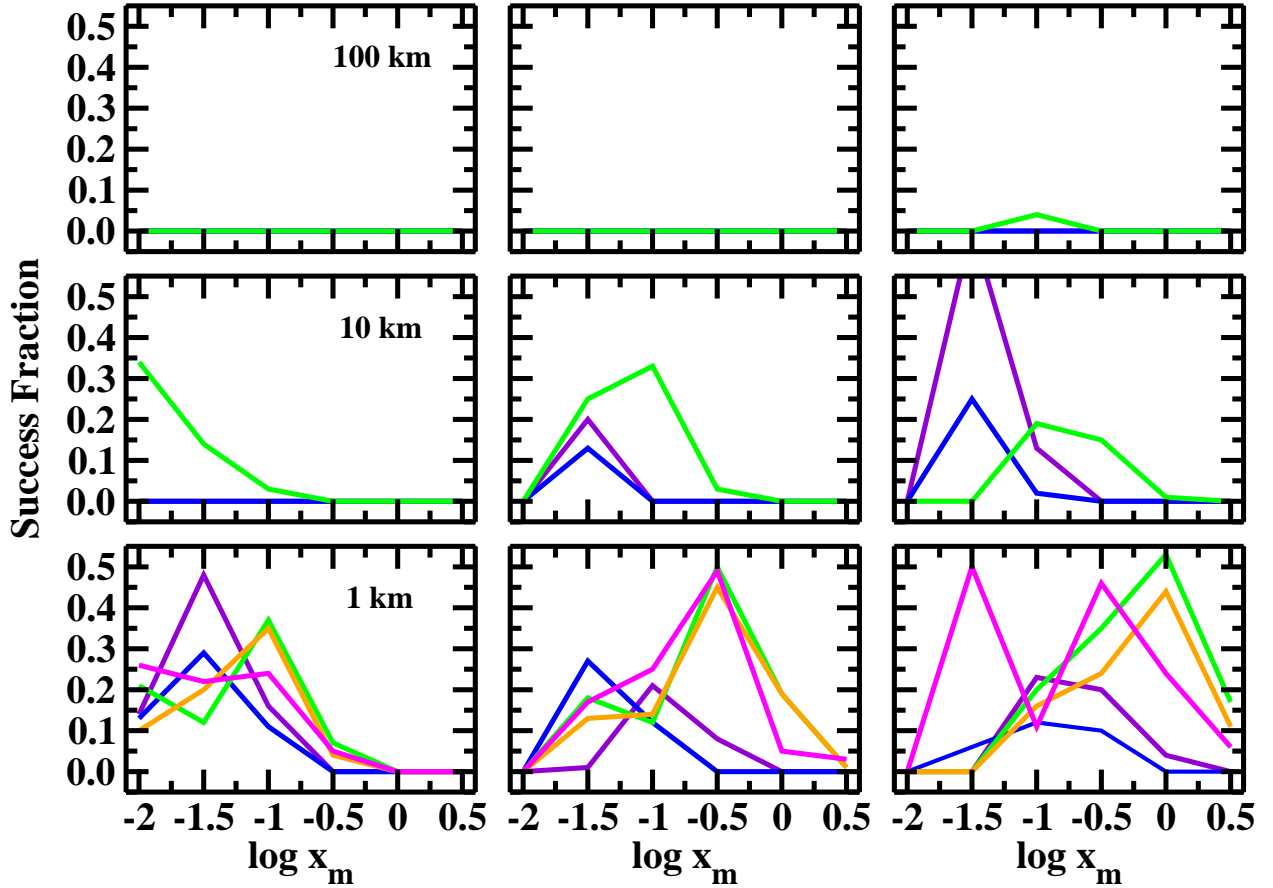


Fig. 15.— As in Fig. 14 for a target slope  $q_4 = 3 \pm 0.25$ . For  $r_0 = 1$  km (lower panels), any range of  $a$ , most initial disk masses, and all fragmentation parameters, 20% to 50% of the calculations reach the target slope and maximum radius; the success rate increases with larger  $r_{max}$ . For  $r_0 = 10$  km, calculations with large disk masses ( $x_m \gtrsim 0.3$ ) reach the target; other calculations fail. For  $r_0 = 100$  km, none of the calculations match the target. In all calculations with  $r_0 = 10$ –100 km, the success rate is independent of  $r_{max}$ .

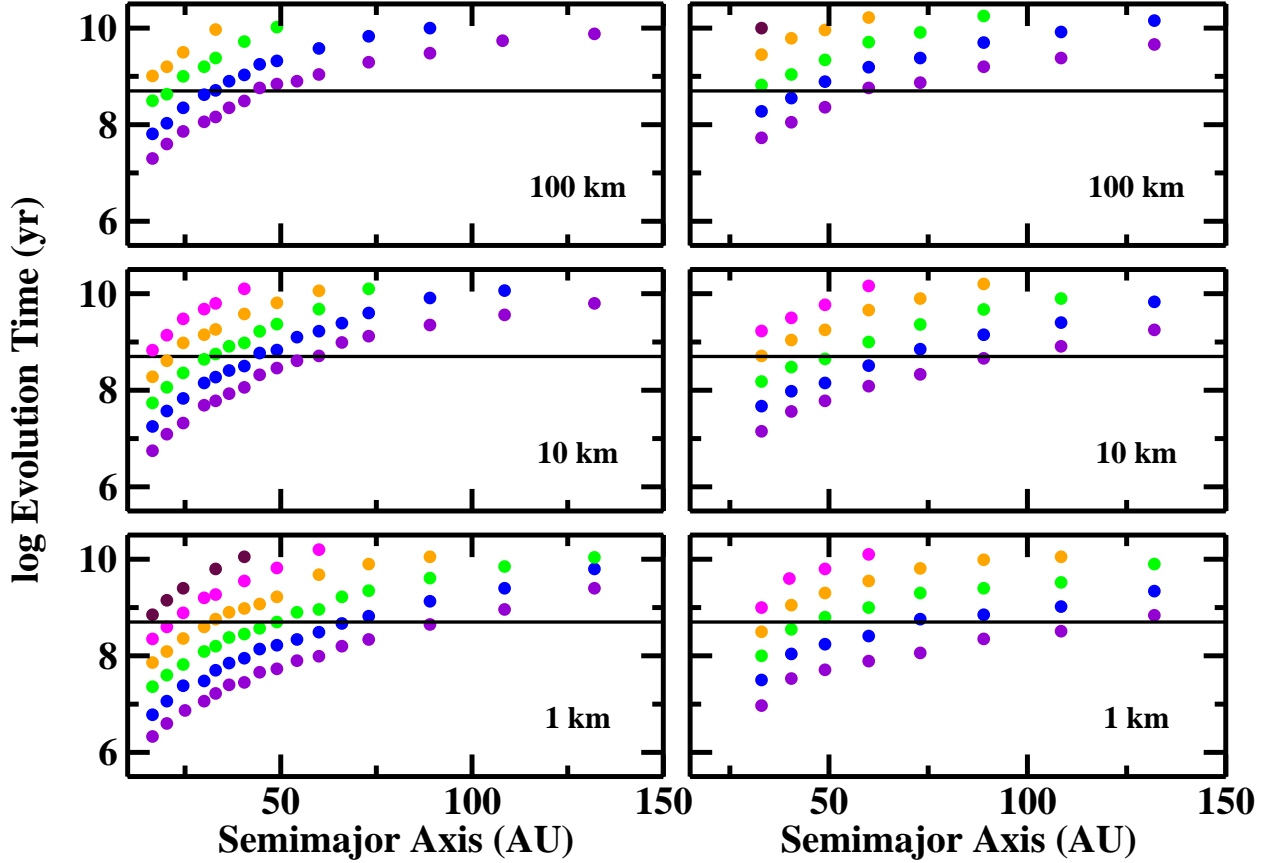


Fig. 16.— The median evolution time to reach  $r_{max} = 1000$  km as a function of semimajor axis for calculations at 15–150 AU with the  $f_w$  fragmentation parameters. Left panels show results for calculations where all of the initial mass is mostly in large planetesimals ( $n_c \propto r^{-0.5}$ ). Right panels show results for calculations where the initial mass is equally distributed in log mass ( $n_c \propto r^{-3}$ ). In each panel, the legend indicates the initial radius of the largest planetesimal. Colored points indicate results for initial values of  $x_m$  from Fig. 6. The black horizontal line illustrates the approximate time of the Late Heavy Bombardment (e.g., Tera et al. 1974; Hartmann et al. 2000; Stöffler & Ryder 2001; Chapman et al. 2007).

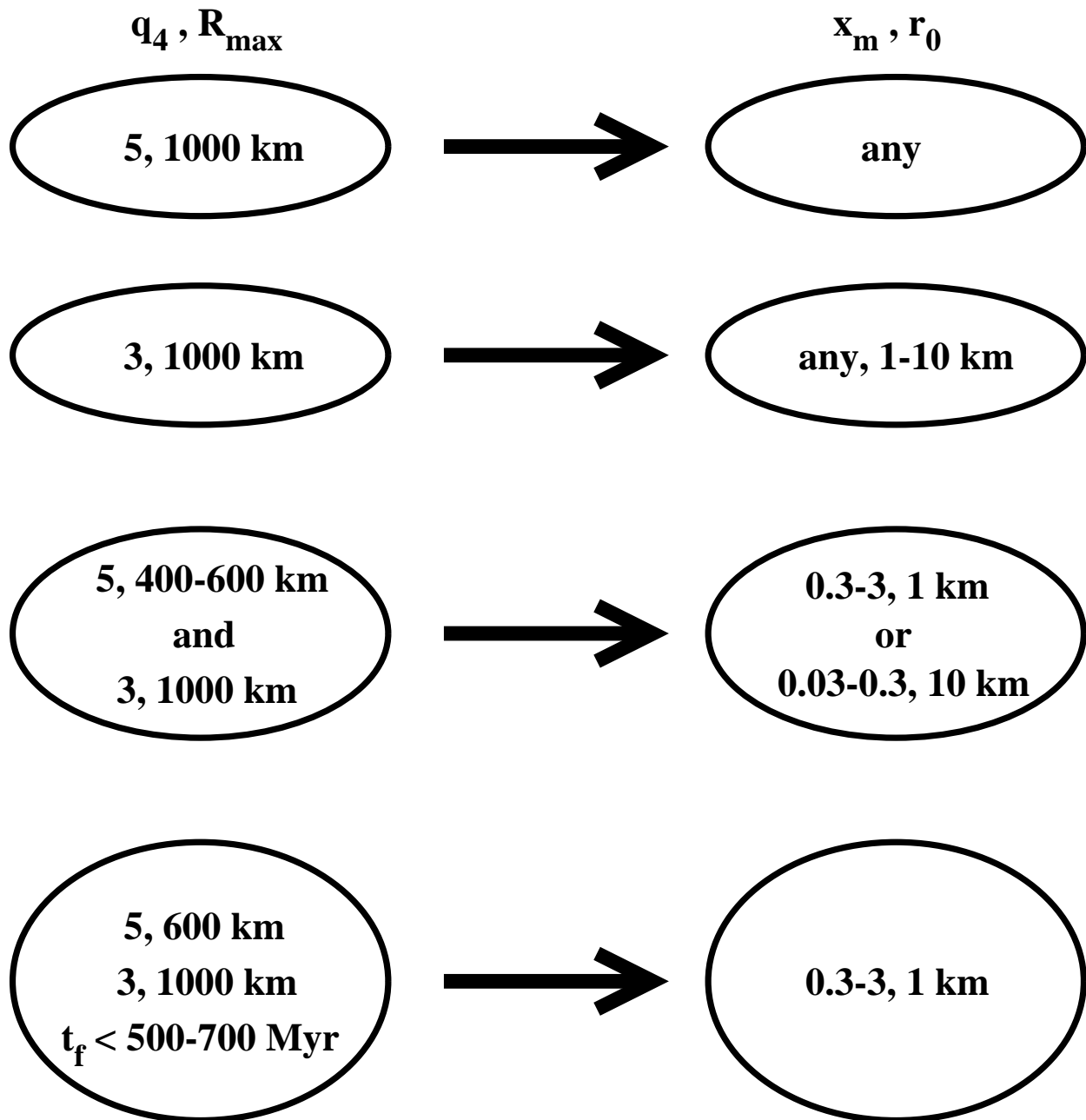


Fig. 17.— Schematic diagram for constraints on coagulation models. The left column lists target values for  $q_4$  and  $r_{\max}$ . The right column lists the constraints on  $x_m$  and  $r_0$ . Individually, measurements of  $q_4$  and  $r_{\max}$  for the cold (first row from top) or the hot (second row) population place few constraints on  $x_m$  or  $r_0$ . Combined (third row), these data limit coagulation models to specific combinations of  $x_m$  and  $r_0$ . When limits on the formation time are added (fourth row), successful models are limited to massive disks with  $r_0 = 1$  km.